Near-Field Antenna Measurement Techniques

Flaminio Ferrara, Claudio Gennarelli, and Rocco Guerriero

Contents

Abstract

A complete description of the near-field antenna measurement techniques is provided in this chapter. After a discussion of the state of the art, the key steps of the classical near-field–far-field (NF-FF) transformations with plane-rectangular, cylindrical, and spherical scannings, in their probe-uncompensated and probe-compensated versions, are summarized, by also providing some analytical details on the wave expansions commonly adopted to represent the antenna radiated field. The nonredundant sampling representations of electromagnetic field are then introduced and applied to drastically reduce the number of required NF data and related measurement time with respect to the classical NF-FF

F. Ferrara • C. Gennarelli (✉) • R. Guerriero
Dipartimento di Ingegneria Industriale, Università di Salerno, Fisciano (Salerno), Italy
e-mail: flferrara@unisa.it; cgennarelli@unisa.it; rguerriero@unisa.it

Z.N. Chen et al. (eds.), *Handbook of Antenna Technologies*,
DOI 10.1007/978-981-4560-44-3_117

transformations. At last, the NF-FF transformations with innovative spiral scannings, allowing a further measurement time saving, are described.

Keywords

Antenna measurements • Near-field – far-field transformation techniques • Plane wave expansion • Cylindrical wave expansion • Spherical wave expansion • Probe compensation • Nonredundant sampling representations of electromagnetic fields • Spiral scannings

Introduction

When dealing with electrically large antennas, far-field (FF) range size limitations, transportation, and mounting problems make it absolutely impractical or impossible to measure their radiation patterns on a conventional FF range. On the other hand, the increasing use of high-performance antennas, as those employed in radar and satellite systems, requires an accurate measure of their radiating characteristics. For instance, satellite antennas are designed to transmit or receive over long distances, and accordingly the requirements to beam pointing may be severe; thus a high measurement accuracy is mandatory to verify that the antenna fulfills all the specifications. As a consequence, the problem of the determination of the antenna FF pattern from near-field (NF) measurements has attracted considerable attention in the last 50 years (Appel-Hansen et al. 1982; Yaghjian 1986; Gillespie 1988; Hald et al. 1988; Gennarelli et al. 2004; Gregson et al. 2007; Francis and Wittmann 2008; Gennarelli et al. 2012; Francis 2012).

NF measurements may be performed in a controlled environment, as an indoor shielded anechoic chamber, which allows one to overcome those drawbacks that, due to weather conditions (rain, snow, etc.), electromagnetic (EM) interference, and other, cannot be eliminated in FF measurements. In addition, NF scanning techniques are the better choice when complete pattern and polarization measurements are required. Moreover, they provide the necessary information to determine the field at the surface of the antenna. Such an information can be properly employed for the diagnostics of surface errors in a reflector antenna or of faulty elements in an array (microwave holographic diagnostics (Yaccarino et al. 1994)).

Another advantage of NF measurements stems from the fact that the reflected signal will be weaker than in a FF measurement facility because it is transmitted and received through far-out sidelobes. Moreover, the absorbers will work more efficiently than in a FF range, where they are employed close to the grazing incidence condition.

It is the authors' opinion that a comprehensive chapter on the NF-FF transformation techniques cannot begin without a preliminary discussion which highlights the field behavior when the distance from the antenna increases. The free space surrounding an antenna is usually subdivided into three regions: the reactive near-field, the radiating near-field, and the far-field region (see Fig. 1). Although no abrupt change in the field behavior can be observed when their boundaries are crossed, the

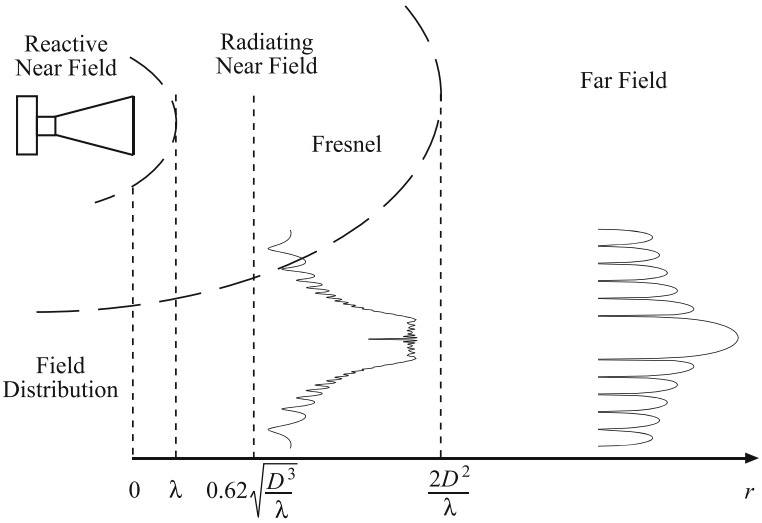

Fig. 1 Field regions of an electrically large antenna

field configuration is quite different in them. For an antenna focused at infinity, the optical term *Fraunhofer region* can be used synonymously with far-field region. For such an antenna, the optical term *Fresnel region* can be also employed to denote a subregion of the radiating near-field zone. The reactive near-field region is the zone immediately surrounding the antenna wherein the reactive field predominates. It extends up to a distance of about $\lambda/2\pi$ from the antenna surface, λ being the wavelength. However, experience with NF measurements indicates that λ is a more reasonable limiting distance for such a region. Outside this zone the reactive field decays rapidly and can be neglected at a distance of a few wavelengths from the antenna surface. The radiating near-field region is the intermediate zone between the reactive near-field and the far-field regions. In such a region the radiation fields predominate, but the angular distribution of the field is dependent on the distance from the antenna, and the field does not exhibit the dependence $e^{-j\beta r}/r$ typical of the antenna far field, β being the wavenumber. It is worthy to note that a time dependence $e^{j\omega t}$ has been implicitly assumed. It will be assumed and suppressed throughout the chapter. The Fresnel region is the radiating near-field subregion wherein a quadratic phase approximation can be used in the vector potential integral. The far-field region is the zone of the free space where the relative angular field distribution is independent of the distance from the antenna and the electric and magnetic fields vary according to the $e^{-j\beta r}/r$ dependence. Commonly, for electrically large antennas, the inner boundaries of the Fraunhofer and Fresnel regions are set at $2D^2/\lambda$ and $0.62\sqrt{D^3/\lambda}$, respectively, where D is the maximum dimension of the antenna. These boundaries are determined by assuming acceptable a maximum phase error of $\pi/8$, when a linear or quadratic phase approximation is used in the expression of the vector potential integral.

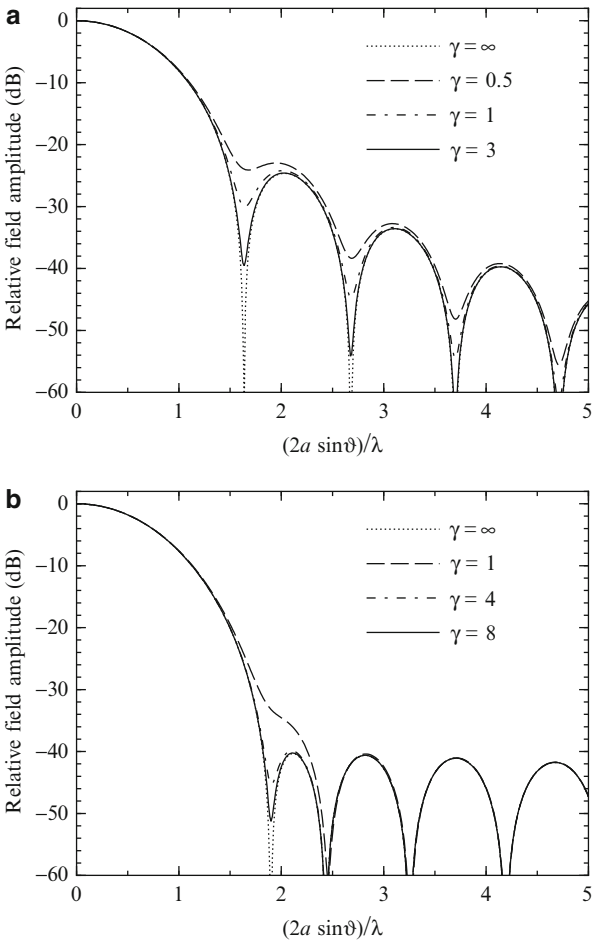

Fig. 2 Pattern behavior referred to the normalized distance $\gamma = r/(2D^2/\lambda)$: (**a**) for a circular aperture with $f(\rho) = (1 - \rho^2)$, (**b**) for a circular Taylor aperture distribution

It has been recognized that distance requirements depend both on first sidelobe level of the antenna and on the desired accuracy (Silver 1984; Hollis et al. 1972). The widely used Rayleigh $2D^2/\lambda$ distance criterion gives rise to negligible pattern errors only for antennas with moderate sidelobe level (−25 dB). When measuring antennas having low (−30 to −40 dB) and ultralow (below −40 dB) sidelobe levels, a distance far larger than $2D^2/\lambda$ is needed (Hansen 1984; Corona et al. 1989). As shown in Fig. 2, particularly for antennas having low sidelobes, a significant increase in the sidelobe level and a more considerable raising of the null between it and the main lobe occur. As a conclusion, the distance requirements for measuring in a FF range the near-in sidelobes, which are below −30 dB, are very severe (Hansen 1984; Corona et al. 1989). For example, a distance of at least $6D^2/\lambda$ is required to measure, within a 1 dB accuracy, the first sidelobe of a Taylor antenna with sidelobe ratio (SLR) = 50 dB.

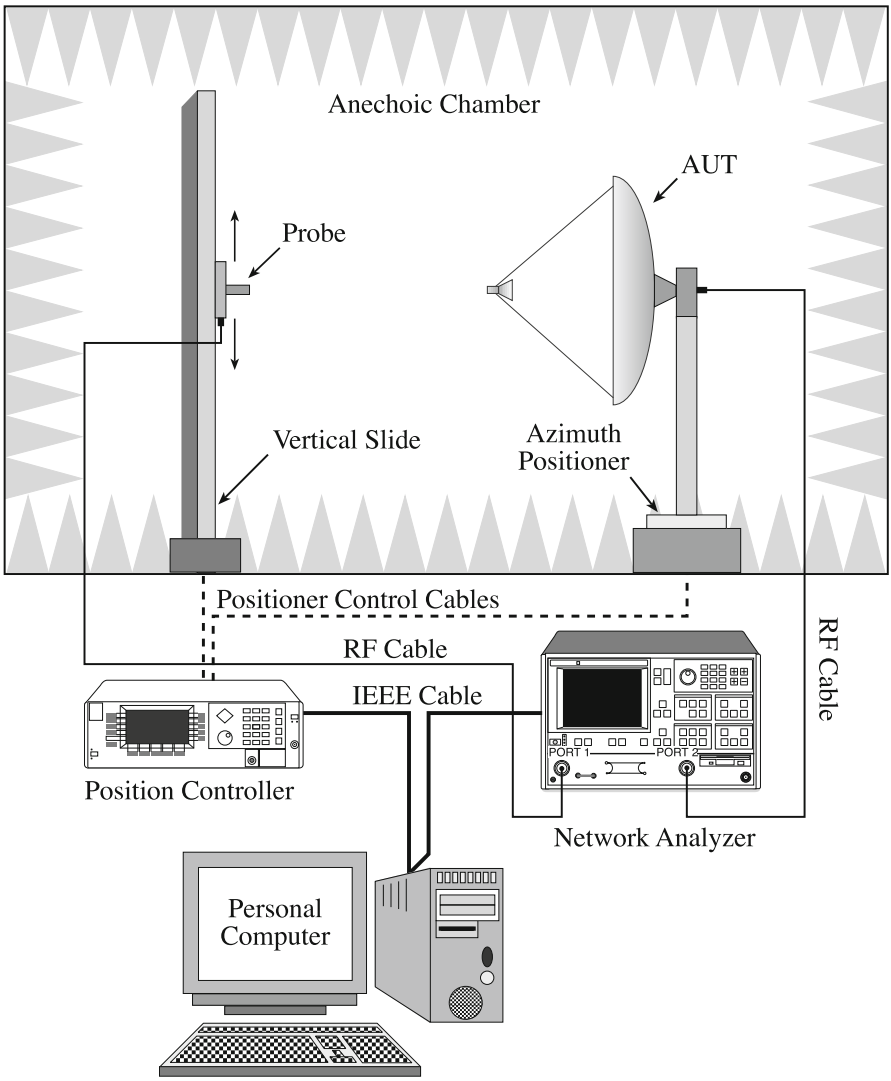

Fig. 3 NF measurement system: cylindrical scanning

Usually, the NF antenna characterization can exploit complex field data or phaseless field data, the first choice being the most commonly used in practice.

In a NF facility processing complex field data, the probe, located near the antenna under test (AUT), is moved through a surface (scanning surface) which can be planar, cylindrical, or spherical (see Fig. 3). It collects complex voltage samples which are stored together with their positions. From these amplitude and phase data, measured for two different orientations of the probe (the probe is rotated by 90° around

its axis in the second set), and taking into account the probe effects, one can compute the antenna FF pattern. It is worth noting that both the copolar and cross-polar components of the antenna far field can be recovered. Moreover, during the NF data acquisition, no information on the AUT polarization is needed. Nevertheless, such an information can be accurately determined by properly processing the reconstructed far field. The probe and its mounting structure should introduce minimum disturbance into the field to be measured, and its characteristics must be stable with time, environmental conditions, and orientations (Francis 2012). Commonly, the measured NF data are transformed into FF patterns by using an expansion of the AUT field in terms of modes, namely, a complete set of solutions of the vector wave equation in the region outside the antenna. Plane, cylindrical, or spherical waves are generally used. The type of modal expansion employed for representing the field determines the kind of the NF scanning surface, which accordingly will be a plane, a cylinder, or a sphere. The orthogonality properties of the modes on such surfaces are then exploited to obtain the modal expansion coefficients, which allow the reconstruction of the AUT far field. The development and the spreading of NF-FF transformation techniques employing planar, cylindrical, or spherical scanning systems is justified from the fact that each approach has its own particular advantages, depending on the AUT and the measurement requirements. The complexity of the analytical transformation increases from the planar to the cylindrical and from the cylindrical to the spherical surfaces.

The NF-FF transformations using a planar scanning are the most simple and efficient ones from the analytical and computational viewpoint. Their main disadvantage is that the pattern can be reconstructed only in a cone with an apex angle less than 180° without repeating the measurements. Accordingly, they are particularly suitable for highly directive antennas which radiate pencil beam patterns. There are quite different ways to realize a planar scanning: plane-rectangular (Kerns 1970, 1981; Joy and Paris 1972; Paris et al. 1978; Joy et al. 1978) (see Fig. 4), plane-polar (Rahmat-Samii et al. 1980; Gatti and Rahmat-Samii 1988; Yaghjian and Woodworth 1996; Bucci et al. 1991a, 1998a, 2000; Fig. 5), and bipolar (Yaccarino et al. 1994; Williams et al. 1994; D'Agostino et al. 2003; Fig. 6).

At the cost of a modest increase in the analytical and computational complication with respect to the planar scannings, the NF-FF transformation with cylindrical scanning (Joy et al. 1978; Leach and Paris 1973; Yaghjian 1977; Appel-Hansen 1980; Bucci et al. 1998b; D'Agostino et al. 2002, 2012a; Qureshi et al. 2013) (see Fig. 7) allows one to reconstruct, from a single set of NF measurements, the AUT complete radiation pattern save for the zones surrounding the spherical polar angles. Such a scanning is particularly attractive when considering antennas that concentrate the EM radiation in an angular region centered on the horizontal plane, as the radiating systems for radio base stations.

The NF-FF transformation with spherical scanning (Hald et al. 1988; Qureshi et al. 2013; Wacker 1975; Larsen 1980; Yaghjian and Wittmann 1985; Hansen 2011; Bucci et al. 2001a; D'Agostino et al. 2011, 2013a) (see Fig. 8) allows one to reconstruct, from a single set of NF measurements, the complete radiation pattern of the AUT. However, the data processing to get the far field is considerably more

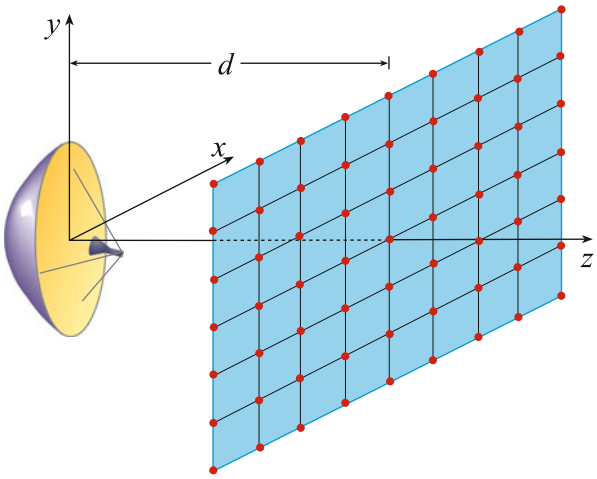

Fig. 4 Plane-rectangular scanning

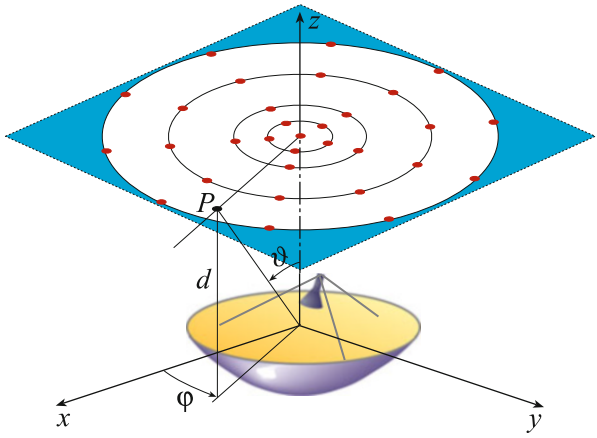

Fig. 5 Plane-polar scanning

complicated than that needed by planar and cylindrical facilities. The NF spherical scanning is, obviously, particularly tailored to measure low-gain and omnidirectional antennas.

In recent years, NF-FF transformations techniques based on the reconstruction of a proper set of equivalent currents have been developed (Petre and Sarkar 1992; Taaghol and Sarkar 1996; Sarkar and Taaghol 1999; Las-Heras and Sarkar 2002; Las-Heras et al. 2006; Alvarez et al. 2008). These (unknown) equivalent currents, lying on a selected surface enclosing the antenna, are evaluated by solving a set of integral equations relating them to the NF data acquired on the scanning surface. Once these equivalent currents have been determined, according to Love's equivalence theorem, it is possible to obtain the field at any point outside the equivalent source domain and, then, to evaluate the FF pattern. Unlike the NF-FF transformations using the modal expansion approach, they do not require the use of canonical

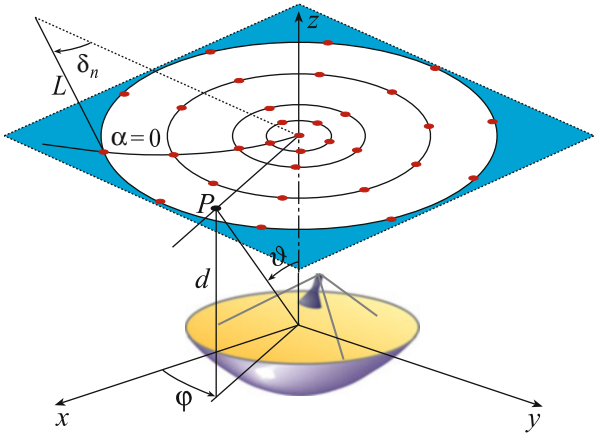

Fig. 6 Bipolar scanning

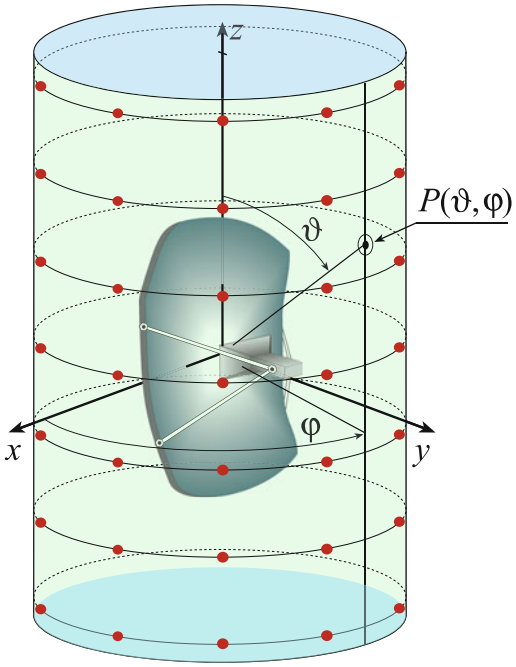

Fig. 7 Cylindrical scanning

scanning surfaces (plane, cylinder, sphere) but can be applied to an arbitrary measurement surface. On the other hand, their main drawback is the remarkably increased computational cost. As a matter of fact, the solution of a system equation (eventually ill-conditioned) with several thousands of unknowns is usually required. It is worthy to note that, for these NF-FF transformations too, it is possible to correct the distortion due to the nonisotropic radiation pattern of the employed probe. The probe correction is obtained by considering the antenna pattern of the probe as a

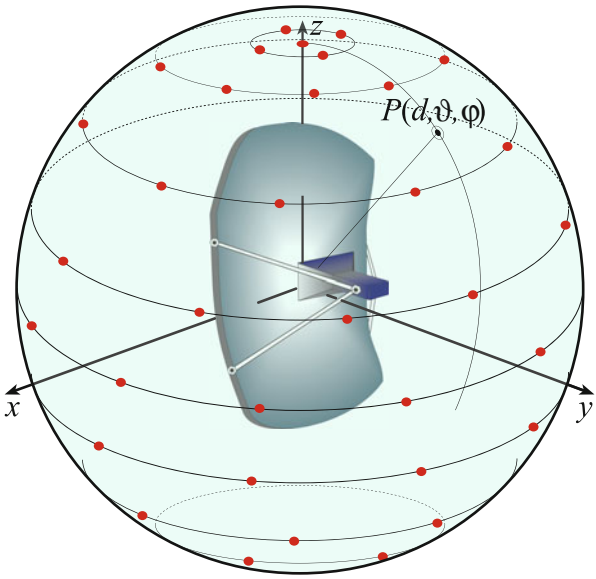

Fig. 8 Spherical scanning

weighting function in the integral equations relating the fields and the equivalent sources (Alvarez et al. 2008).

As already stressed, near-field techniques usually require the measurement of both the amplitude and phase of the antenna near field. Nevertheless, phaseless NF measurements have recently attracted a considerable interest, due to the less expensive measurement facilities required and to the increasing difficulty to perform accurate phase measurements in the millimeter and submillimeter frequency range. Over the years, several techniques have been proposed to determine the antenna far field from only amplitude NF measurements. A first possibility is the use of interferometric techniques (Bennett et al. 1976), which require an additional reference antenna whose transmitted signal, interfering with that transmitted by the AUT, allows to recover the lacking phase information. Other approaches exploit the functional relationship existing between two sets of only amplitude NF data collected by a probe on two scanning surfaces (Bucci et al. 1990, 1999; Isernia et al. 1996; Yaccarino and Rahmat-Samii 1999) or by two probes on the same scanning surface (Pierri et al. 1999) to retrieve the phase. A basically interferometric approach, avoiding the use of a reference antenna and using two identical probes and a simple microstrip circuit, has been also proposed to retrieve the phase information (Costanzo and Di Massa 2002; Costanzo et al. 2005).

Each member of the antenna measurement techniques community can profit today by about 50 years of research activity on NF data acquisition and related NF-FF transformations. Over these years, many solutions have been proposed to meet the demands of the various applications. In this framework, significant improvements in the performance of NF measurements have been recently achieved. They are based on the spatial band limitation properties of radiated EM fields

(Bucci and Franceschetti 1987, 1989), on their nonredundant sampling representations (Bucci et al. 1998c; Bucci and Gennarelli 2012), and on the optimal sampling interpolation (OSI) expansions of central type (Bucci et al. 1991a, b; Gennarelli et al. 1994). In particular, a significant reduction of the number of required NF data (and, as a consequence, of the corresponding measurement time) has been obtained for all the conventional scannings (see (Bucci et al. 1991a, 1998a, 2000) for the plane-polar, (D'Agostino et al. 2003) for the bipolar, (Bucci et al. 1998b; D'Agostino et al. 2002, 2012a) for the cylindrical, and (Bucci et al. 2001a; D'Agostino et al. 2011, 2013a) for the spherical scanning). In fact, the NF data needed by the corresponding traditional NF-FF transformation technique are accurately recovered by interpolating a minimum set of measurements via OSI expansions. A remarkable measurement time saving can be so obtained making these nonredundant transformations more and more appealing, since nowadays such a time is very much greater than the computational one. The mathematical justification for these results relies on the abovementioned band limitation properties and nonredundant sampling representations of EM fields. In fact, the EM fields radiated by antennas, enclosed in a convex domain bounded by a rotational surface Σ and observed on surface $\mathcal{M}$ with the same rotational symmetry, can be very well approximated by spatially band-limited functions when a proper phase factor is singled out from the field expression and proper parameterizations are used to describe $\mathcal{M}$ (Bucci et al. 1998c). Since the voltage acquired by a nondirective probe has the same effective spatial bandwidth of the AUT field, these representations can be, obviously, applied to the voltage too. The application of these nonredundant sampling representations has allowed also the development of an innovative and efficient planar NF-FF transformation using the planar wide-mesh scanning (PWMS) (Ferrara et al. 2007; D'Agostino et al. 2014a). Such a nonconventional plane-rectangular scanning technique is so named, since the sample grid is characterized by meshes wider and wider when going away from the center of the scanning region (see Fig. 9).

The use of the modulated scattering technique employing arrays of scattering probes, which allows a very fast electronic scanning, has been also proposed in (Bolomey et al. 1988) to reduce the time required for the acquisition of the NF data. However, apart from measurement precision issues, antenna testing facilities based on such a technique are not very flexible. Anyway, exploitation of the nonredundant sampling representations could allow to reduce the number of needed probes.

A more viable way to reduce the time required for the NF data acquisition is the employment of innovative spiral scanning techniques. They have been implemented, as suggested in (Yaccarino et al. 1996), by means of continuous and synchronized movements of the positioning systems of the probe and AUT. Accurate, stable, and efficient NF-FF transformations with helicoidal (Bucci et al. 2001b; D'Agostino et al. 2008a, 2009a, b, 2012b) (see Fig. 10), planar (Bucci et al. 2002; D'Agostino et al. 2008b; Fig. 11), and spherical (Bucci et al. 2003; D'Agostino et al. 2009c, 2012c, 2013b, 2014b; Fig. 12) spiral scanning have been developed in the last years. They rely on nonredundant sampling representations and reconstruct the NF data needed by the classical NF-FF transformation corresponding to the adopted scanning

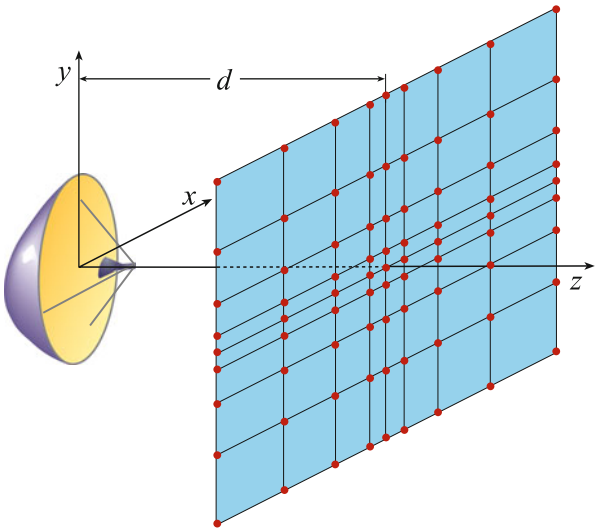

Fig. 9 Planar wide-mesh scanning

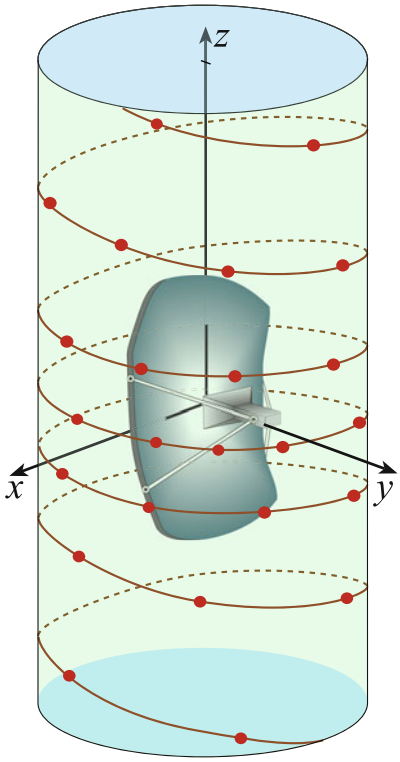

Fig. 10 Helicoidal scanning

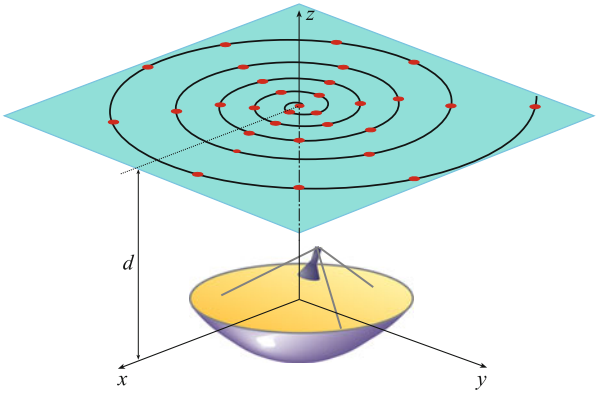

Fig. 11 Planar spiral scanning

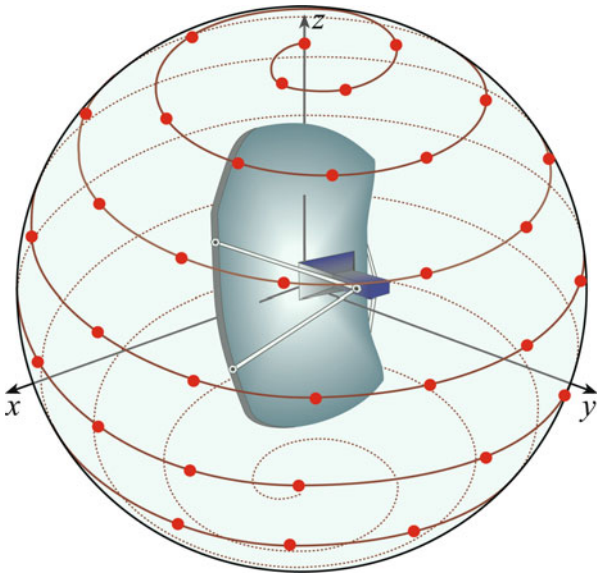

Fig. 12 Spherical spiral scanning

surface, by interpolating, via appropriate OSI formulas, the nonredundant samples acquired by the measurement probe on the considered curve (helix or spiral). Other NF-FF transformation techniques with spiral scannings have been also proposed (Yaccarino et al. 1996; Costanzo and Di Massa 2004, 2007). However, since these approaches do not exploit the nonredundant representations of EM fields, they need a useless large amount of NF measurements.

The chapter is organized as follows. The classical NF-FF transformations with plane-rectangular, cylindrical, and spherical scannings, in their probe-uncompensated and probe-compensated versions, are summarized in section "Classical NF-FF Transformation Techniques." The nonredundant sampling

representations of the electromagnetic fields are introduced in section "Nonredundant NF-FF Transformation Techniques," highlighting the role of the optimal parameterization and phase factor. In the same section, the application of these representations to the NF-FF transformations with conventional scannings, allowing a drastic measurement time saving, is also described. The theoretical foundations of the NF-FF transformations with spiral scanning for both quasispherical antennas (D'Agostino et al. 2006, 2009d) and those having two dimensions very different from the third one (D'Agostino et al. 2009e; Cicchetti et al. 2014) are presented in the subsequent section "NF-FF Transformation Techniques with Spiral Scannings" by providing an efficient sampling representation, which allows the reconstruction of the EM field (probe voltage) on a quite arbitrary rotational surface from a nonredundant number of its samples collected on a spiral wrapping it.

Classical NF-FF Transformation Techniques

NF-FF Transformation with Plane-Rectangular Scanning

The NF-FF transformation with plane-rectangular scanning (see Fig. 4) is without doubt the most simple and efficient one from the analytical and computational viewpoints. Its main drawback is that the antenna far field can be reconstructed only in a cone with an apex angle less than 180°. Therefore, it can be conveniently employed for highly directive antennas which radiate pencil beam patterns well within the solid angle specified by the edges of the AUT and those of the scanning area. In the plane-rectangular scanning, the probe is mounted on a $x - y$ positioner so that it can acquire the NF amplitude and phase data on the wanted plane-rectangular grid. From these data, measured for two different orientations of the probe, one can compute the FF pattern of the AUT (Kerns 1970, 1981; Joy and Paris 1972; Paris et al. 1978; Joy et al. 1978).

In the first part of this subsection, the use of an ideal probe able to measure in its two orientations the tangential components E_x, E_y of the AUT electric field on the scanning plane is assumed and NF-FF transformation formulas derived. Then, such a hypothesis is removed and probe-corrected formulas given.

The starting point is the plane wave spectrum representation of EM fields (Clemmow 1966), summarized in the paragraph "Plane Wave Expansion" for readers' convenience. As shown in it, the tangential components E_x, E_y of the electric field radiated by the AUT can be represented on the scan plane at $z = d$ as a superposition of elementary plane waves, i.e.,

$$\mathbf{E}_{x,y}(x,y,d) = \int_{-\infty}^{+\infty}\int_{-\infty}^{+\infty} \left[\mathbf{E}_{x,y}(k_x,k_y)\mathrm{e}^{-\mathrm{j}k_z d}\right]\mathrm{e}^{-\mathrm{j}\left(k_x x + k_y y\right)}\mathrm{d}k_x\mathrm{d}k_y \tag{1}$$

By Fourier inverse transforming, it results

$$\mathbf{E}_{x,y}(k_x, k_y) = \frac{1}{4\pi^2} e^{jk_z d} \int_{-\infty}^{+\infty} \int_{-\infty}^{+\infty} \mathbf{E}_{x,y}(x, y, d) e^{j(k_x x + k_y y)} dx dy \tag{2}$$

Accordingly, by assuming that the tangential components of the electric field are zero out of the measurement region on the scanning plane, it is possible to obtain the x and y components of the plane wave spectrum by a two-dimensional fast Fourier transform (FFT) algorithm. The other component of the spectrum can be determined by means of Eq. 75.

As shown in (Joy and Paris 1972), the sample spacings of the NF data are

$$\Delta x \leq \lambda/2; \quad \Delta y \leq \lambda/2 \tag{3}$$

In fact, if the scanning plane is located in a region of space where the EM field does not contain evanescent waves, then the plane wave spectrum is zero for $|k_x| > 2\pi/\lambda$ and $|k_y| > 2\pi/\lambda$. As a consequence of the two-dimensional Nyquist sampling theorem (Papoulis 1987), the EM field on the plane $z = d$ can be reconstructed from the knowledge of its samples at a rectangular lattice of points separated by grid spacings satisfying Eq. 3.

Once the plane wave spectrum has been determined, the FF components of the electric field in the spherical coordinate system (r, ϑ, φ) can be evaluated (see paragraph "Plane Wave Expansion") by using the relations

$$\mathbf{E}_\vartheta(r, \vartheta, \varphi) = j2\pi\beta \cos\vartheta \mathbf{E}_\vartheta(\beta \sin\vartheta \cos\varphi, \beta \sin\vartheta \sin\varphi) \frac{e^{-j\beta r}}{r} \tag{4}$$

$$\mathbf{E}_\varphi(r, \vartheta, \varphi) = j2\pi\beta \cos\vartheta \mathbf{E}_\varphi(\beta \sin\vartheta \cos\varphi, \beta \sin\vartheta \sin\varphi) \frac{e^{-j\beta r}}{r} \tag{5}$$

where $\mathbf{E}_\vartheta$, $\mathbf{E}_\varphi$ are related to $\mathbf{E}_x$ and $\mathbf{E}_y$ by

$$\mathbf{E}_\varphi = -\mathbf{E}_x \sin\varphi + \mathbf{E}_y \cos\varphi \tag{6}$$

$$\mathbf{E}_\vartheta = (\mathbf{E}_x \cos\varphi + \mathbf{E}_y \sin\varphi) / \cos\vartheta \tag{7}$$

As a matter of fact,

$$\mathbf{E}_\vartheta = \mathbf{E}_x \cos\vartheta \cos\varphi + \mathbf{E}_y \cos\vartheta \sin\varphi - \mathbf{E}_z \sin\vartheta$$

from which, by taking into account Eq. 75, Eq. 7 is easily obtained.

It is convenient to describe the employment of the FFT algorithm for computing the two-dimensional Fourier transforms in Eq. 2 from the knowledge of the acquired

NF data. It can be useful to remember (Brigham 1974) that the discrete Fourier transform (DFT) is defined by

$$G\left(\frac{n}{NT}\right) = \sum_{i=0}^{N-1} g(iT)\mathrm{e}^{-\mathrm{j}2\pi ni/N} \quad n = 0, 1, \ldots, N-1 \tag{8}$$

whereas the inverse discrete Fourier transform (IDFT) is given by

$$g(iT) = \frac{1}{N}\sum_{n=0}^{N-1} G\left(\frac{n}{NT}\right)\mathrm{e}^{\,\mathrm{j}2\pi ni/N} \quad i = 0, 1, \ldots, N-1 \tag{9}$$

As well known, Eqs. 8 and 9 can be efficiently computed via the FFT algorithm. Moreover, they require both the functions to be periodic, namely,

$$G\left(\frac{n+pN}{NT}\right) = G\left(\frac{n}{NT}\right) \quad p = 0, \pm 1, \pm 2, \ldots \tag{10}$$

$$g[(i+pN)T] = g(iT) \quad p = 0, \pm 1, \pm 2, \ldots \tag{11}$$

The integration along x in Eq. 2 is now considered. By taking into account explicitly the truncation due to the finite size $2L_x \times 2L_y$ of the scanning plane and applying a straightforward approximation, it results

$$G(k_x) = \int_{-L_x}^{L_x} g(x)\mathrm{e}^{\mathrm{j}k_x x}\mathrm{d}x \approx \Delta x \sum_{n=0}^{N_x-1} g(x_n)\mathrm{e}^{\mathrm{j}k_x(n-N_x/2)\Delta x} \tag{12}$$

where $x_n = (n - N_x/2)\Delta x$, $N_x = 2L_x/\Delta x$ is the number of the measurement points along x (the overall number of measurement points is N_xN_y). When evaluating $G(k_x)$ at $k_{x_i} = i\Delta k_x = 2\pi i/(N_x\Delta x)$, it results

$$G(k_{x_i}) \approx \frac{2L_x}{N_x}\mathrm{e}^{-\mathrm{j}\pi i}\sum_{n=0}^{N_x-1} g(x_n)\mathrm{e}^{\mathrm{j}2\pi ni/N_x} \tag{13}$$

Accordingly, the integration over x in Eq. 2 can be efficiently performed via an inverse FFT algorithm, provided that the so obtained results are multiplied by the factor $2L_x\mathrm{e}^{-\mathrm{j}\pi i}$. The same considerations can be, obviously, applied to the integration over y.

Summing up, for the evaluation of each of the Cartesian components $\mathbf{E}_x$ and $\mathbf{E}_y$ of the spectrum are needed N_y one-dimensional FFTs of size N_x and N_x FFTs of size N_y. This allows to obtain the FF components at the values of k_x and k_y given by $k_{x_i} = 2$

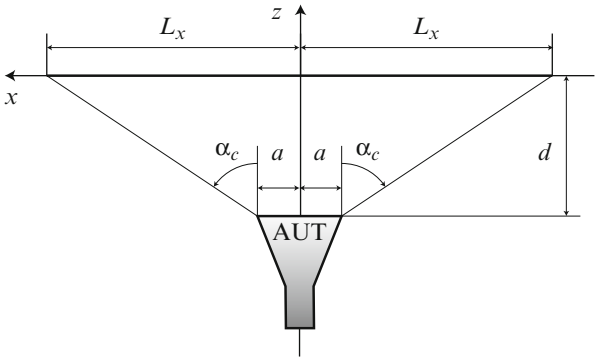

Fig. 13 Relevant to the evaluation of the validity angle

$\pi i/(N_x \Delta x)$ and $k_{y_p} = 2\pi p/(N_y \Delta y)$. Note that the k_x and k_y vales such that $k_x^2 + k_y^2 > \beta^2$ must not be considered since the corresponding plane waves (called evanescent waves) do not contribute to the far field and represent NF reactive power storage.

To obtain the FF components with a greater resolution, it is sufficient "zero-filling" the NF data. Namely, to increase the number of output k_x values from N_x to N_x', the NF data must be increased with a proper number of zeros corresponding to fictitious $(N_x' - N_x)/2$ measurement points both before and after the effective ones. Similarly, to increase the number of output k_y values from N_y to N_y', $\left(N_y' - N_y\right)/2$ zeros must be added before and after the measured ones.

Since the measurement region is truncated in the plane-rectangular scanning, the reconstructed far field is affected by an inevitable truncation error, whose amount depends on the level of the neglected NF data external to the scanning area. In the following, the effect of the truncation due to the finite extension of the scanning plane along the x direction is analyzed. Quite analogous results hold also for that relevant to the y direction. When considering a scanning plane at distance d from the AUT, whose dimension along x is $2a$ (see Fig. 13), a convenient rule of thumb to predict the angular region of validity of the recovered FF pattern is given (Newell 1988) by

$$-\alpha_c \leqslant \vartheta \leqslant \alpha_c \tag{14}$$

where

$$\alpha_c = \tan^{-1}\left(\frac{L_x - a}{d}\right) \tag{15}$$

Such a validity angular region criterion was developed empirically from extensive NF measurements involving a large number of antenna and probe combinations (Yaghjian 1975) and derived using a theoretical analysis (Newell and Crawford 1974). Moreover, a ripple caused by the discontinuity of the near field at the edges of the scanning plane can appear even in the region of validity (Newell 1988).

It can be easily recognized that the NF tangential components E_x, E_y cannot be acquired when performing the measurement by means of a real, not ideal, probe. In fact, the probe sees the AUT center under different directions when moving on the scanning plane. Moreover, also at a fixed position, it sees each portion of the AUT under a different direction. As a consequence, the antenna far field cannot be accurately recovered from the measured NF data by employing the previously described uncompensated NF-FF transformation.

The basic theory of probe-compensated NF measurements on a plane as proposed in (Paris et al. 1978; Joy et al. 1978) is based on the application of the Lorentz reciprocity theorem. The key relations in the here adopted reference system are

$$E_\vartheta(\vartheta,\varphi) = \left(I_H E'_{\varphi_V}(\vartheta, -\varphi) - I_V E'_{\varphi_H}(\vartheta, -\varphi)\right)/\Delta \tag{16}$$

$$E_\varphi(\vartheta,\varphi) = \left(I_H E'_{\vartheta_V}(\vartheta, -\varphi) - I_V E'_{\vartheta_H}(\vartheta, -\varphi)\right)/\Delta \tag{17}$$

where

$$\Delta = E'_{\vartheta H}(\vartheta, -\varphi)E'_{\varphi_V}(\vartheta, -\varphi) - E'_{\vartheta_V}(\vartheta, -\varphi)E'_{\varphi_H}(\vartheta, -\varphi) \tag{18}$$

and

$$I_{V,H} = A\cos\vartheta\ \mathrm{e}^{\mathrm{j}\beta d\cos\vartheta}\int_{-\infty}^{+\infty}\int_{-\infty}^{+\infty} V_{V,H}(x,y)\mathrm{e}^{\mathrm{j}\beta x\sin\vartheta\cos\varphi}\mathrm{e}^{\mathrm{j}\beta y\sin\vartheta\sin\varphi}\mathrm{d}x\ \mathrm{d}y \tag{19}$$

A being a proper constant. Namely, the antenna far field is related to (i) the two-dimensional Fourier transforms of the output voltages V_V and V_H of the probe for two independent sets of measurements (the probe is rotated by 90° in the second set); (ii) the FF components E'_{ϑ_V}, E'_{φ_V} and E'_{ϑ_H}, E'_{φ_H} radiated by the probe and the rotated probe when used as transmitting antennas.

In the following, a simple demonstration of the probe-compensated NF-FF transformation with plane-rectangular scanning is given. It is valid in the hypothesis that the mutual coupling effects be negligible and the AUT and probe be reciprocal. By expressing the electric field radiated by the AUT and impinging on the probe as superposition of elementary plane waves (see Eq. 80) and taking into account the relations between the AUT and the probe coordinate systems (see Fig. 14), it can be easily verified that the open circuit voltage at the probe terminals is given by

$$V(\underline{r}) = \int_{-\infty}^{+\infty}\int_{-\infty}^{+\infty} \underline{\mathbf{E}}(k_x,k_y)\cdot\underline{h}(k_x, -k_y)\mathrm{e}^{-\mathrm{j}\underline{k}\cdot\underline{r}}\mathrm{d}k_x\mathrm{d}k_y \tag{20}$$

where $\underline{h}$ is the receiving effective length of the probe and the symbol $(\cdot)$ denotes the inner product. By Fourier inverse transforming Eq. 20, it results

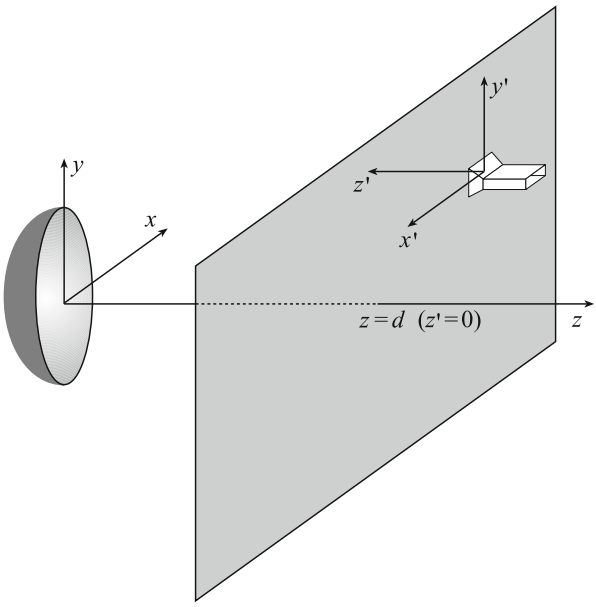

Fig. 14 Geometry relevant to the probe compensation

$$\underline{\mathbf{E}}(k_x, k_y) \cdot \underline{h}(k_x, -k_y) = \frac{1}{4\pi^2} \mathrm{e}^{\mathrm{j}k_z d} \int_{-\infty}^{+\infty} \int_{-\infty}^{+\infty} V(x,y) \mathrm{e}^{\mathrm{j}(k_x x + k_y y)} \mathrm{d}x\mathrm{d}y \tag{21}$$

For a reciprocal antenna the receiving and transmitting effective lengths coincide, and thus, by expressing the electric field $\underline{E}'$ radiated by the probe in the FF region as function of probe effective length (Franceschetti 1997)

$$\underline{E}' = \mathrm{j}\frac{\zeta}{2\lambda r} I_0 \mathrm{e}^{-\mathrm{j}\beta r} \underline{h} \tag{22}$$

where ζ is the free-space impedance and I_0 is the antenna input current, it results

$$\underline{\mathbf{E}}(k_x, k_y) \cdot \underline{E}'(k_x, -k_y) = \frac{\mathrm{j}\zeta I_0 \mathrm{e}^{-\mathrm{j}\beta r}}{2\lambda r} \frac{\mathrm{e}^{\mathrm{j}k_z d}}{4\pi^2} \int_{-\infty}^{+\infty} \int_{-\infty}^{+\infty} V(x,y) \mathrm{e}^{\mathrm{j}(k_x x + k_y y)} \mathrm{d}x\mathrm{d}y \tag{23}$$

This last, by taking into account Eq. 81, becomes

$$\underline{E}(\vartheta, \varphi) \cdot \underline{E}'(\vartheta, -\varphi) = -\frac{2\pi\beta\zeta I_0 \mathrm{e}^{-\mathrm{j}2\beta r}}{2\lambda r^2} \frac{\mathrm{e}^{\mathrm{j}\beta d \cos\vartheta}}{4\pi^2} \cos\vartheta \int_{-\infty}^{+\infty} \int_{-\infty}^{+\infty} V(x,y) \mathrm{e}^{\mathrm{j}(k_x x + k_y y)} \mathrm{d}x\mathrm{d}y \tag{24}$$

This last can be rewritten in a more convenient form by considering that the following relations between the AUT and the probe reference systems (see Fig. 14) hold:

$$\vartheta' = \vartheta; \quad \varphi' = -\varphi; \quad \hat{\vartheta}' = -\hat{\vartheta}; \quad \hat{\varphi}' = \hat{\varphi} \tag{25}$$

By properly taking into account these last, it is possible to rewrite Eq. 24 in terms of the spherical components of the field quantities, thus getting

$$\begin{aligned} &E_\vartheta(\vartheta,\varphi)E'_\vartheta(\vartheta,\,-\varphi) - E_\varphi(\vartheta,\varphi)E'_\varphi(\vartheta,\,-\varphi) \\ &\quad = A\cos\vartheta\ \ \mathrm{e}^{\mathrm{j}\beta d\cos\vartheta}\int_{-\infty}^{+\infty}\int_{-\infty}^{+\infty} V(x,y)\ \ \mathrm{e}^{\mathrm{j}\beta x\sin\vartheta\cos\varphi}\mathrm{e}^{\mathrm{j}\beta y\sin\vartheta\sin\varphi}\mathrm{d}x\mathrm{d}y \end{aligned} \tag{26}$$

where

$$A = \frac{1}{4\pi^2}\frac{2\pi\beta\zeta I_0\mathrm{e}^{-\mathrm{j}2\beta r}}{2\lambda r^2}$$

From Eq. 26, by assuming to perform two independent sets of measurements (the probe is rotated by 90° around its axis z' in the second set), the following linear system is obtained:

$$E_\vartheta(\vartheta,\varphi)E'_{\vartheta_V}(\vartheta,\,-\varphi) - E_\varphi(\vartheta,\varphi)E'_{\varphi_V}(\vartheta,\,-\varphi) = I_V \tag{27}$$

$$E_\vartheta(\vartheta,\varphi)E'_{\vartheta_H}(\vartheta,\,-\varphi) - E_\varphi(\vartheta,\varphi)E'_{\varphi_H}(\vartheta,\,-\varphi) = I_H \tag{28}$$

By solving such a system, Eqs. 16 and 17 are finally got.

NF-FF Transformation with Cylindrical Scanning

The NF-FF transformation with cylindrical scanning (see Fig. 7) allows one to reconstruct, from a single set of NF measurements, the antenna complete radiation pattern save for the zones surrounding the spherical polar angles and, accordingly, is particularly tailored for antennas that radiate mainly in an angular region centered on the horizontal plane. This, however, is obtained at the cost of a moderate increase in the analytical and computational complication with respect to that using the plane-rectangular scanning. In a cylindrical scanning facility, the AUT is mounted on a rotating table, whereas the probe moves along a line parallel to the rotation axis of the table. By properly matching these movements, the probe can acquire the NF amplitude and phase data on the wanted cylindrical grid. From these data, measured for two different orientations of the probe and accounting for the probe effects, the

FF pattern can be evaluated (Joy et al. 1978; Leach and Paris 1973; Yaghjian 1977). As done in the plane-rectangular case, probe-uncorrected NF-FF transformation formulas, valid in the ideal probe assumption, are initially derived. Then, such an assumption is removed and probe-compensated formulas given.

As well known, in the cylindrical coordinate system (ρ, φ, z), the tangential components of the electric field radiated by the AUT can be represented (Leach and Paris 1973) on the scanning cylinder as a superposition of elementary cylindrical waves (see paragraph "Cylindrical Wave Expansion"), namely,

$$E_z(\varphi, z) = \sum_{\nu=-\infty}^{\infty} \int_{-\infty}^{\infty} b_\nu(\eta) \frac{\Lambda^2}{\beta} H_\nu^{(2)}(\Lambda d) \mathrm{e}^{\mathrm{j}\nu\varphi} \mathrm{e}^{-\mathrm{j}\eta z} \mathrm{d}\eta \tag{29}$$

$$E_\varphi(\varphi, z) = \sum_{\nu=-\infty}^{\infty} \int_{-\infty}^{\infty} \left[b_\nu(\eta) \frac{\nu\eta}{\beta d} H_\nu^{(2)}(\Lambda d) - a_\nu(\eta) \frac{\partial}{\partial\rho} H_\nu^{(2)}(\Lambda\rho) \Big|_{\rho=d} \right] \mathrm{e}^{\mathrm{j}\nu\varphi} \mathrm{e}^{-\mathrm{j}\eta z} \mathrm{d}\eta \tag{30}$$

where d is the cylinder radius, a_ν and b_ν are the modal expansion coefficients, $H_\nu^{(2)}(\cdot)$ is the Hankel function of second kind of order ν, and $\Lambda = (\beta^2 - \eta^2)^{1/2}$.

The modal coefficients are determined by Fourier inverse transforming Eqs. 29 and 30, thus obtaining

$$b_\nu(\eta) \frac{\Lambda^2}{\beta} H_\nu^{(2)}(\Lambda d) = \frac{1}{4\pi^2} \int_{-\infty}^{\infty} \int_{-\pi}^{\pi} E_z(\varphi, z) \mathrm{e}^{-\mathrm{j}\nu\varphi} \mathrm{e}^{\mathrm{j}\eta z} \mathrm{d}\varphi \, \mathrm{d}z \tag{31}$$

$$b_\nu(\eta) \frac{\nu\eta}{\beta d} H_\nu^{(2)}(\Lambda d) - a_\nu(\eta) \frac{\partial}{\partial\rho} H_\nu^{(2)}(\Lambda\rho) \Big|_{\rho=d} = \frac{1}{4\pi^2} \int_{-\infty}^{\infty} \int_{-\pi}^{\pi} E_\varphi(\varphi, z) \mathrm{e}^{-\mathrm{j}\nu\varphi} \mathrm{e}^{\mathrm{j}\eta z} \mathrm{d}\varphi \mathrm{d}z \tag{32}$$

In the classical approach (Leach and Paris 1973), the FFT is employed to evaluate the modal coefficients in an efficient way, and the sample spacings of the NF data are

$$\Delta z \leqslant \lambda/2; \quad \Delta\varphi \leqslant \pi/(\beta a') = \lambda/(2a') \tag{33}$$

where a' is the radius of the smallest cylinder enclosing the AUT. In fact, if the scanning cylinder is located in a region of space where the EM field does not contain evanescent waves, then the cylindrical wave coefficients are zero for $|\eta| > \beta$ and $|\nu| > \beta a'$. As a consequence of the two-dimensional Nyquist sampling theorem (Papoulis 1987), the EM field on the cylinder at $\rho = d$ can be reconstructed from the knowledge of its samples at a regular lattice of points separated by grid spacings satisfying Eq. 33.

Once the modal coefficients are determined, the FF components of the electric field in the spherical coordinate system (r, ϑ, φ) can be evaluated (see paragraph "Cylindrical Wave Expansion") by

$$E_{\vartheta}(r,\vartheta,\varphi) = -\mathrm{j}2\beta\frac{\mathrm{e}^{-\mathrm{j}\beta r}}{r}\sin\vartheta\sum_{\nu=-\infty}^{\infty}\mathrm{j}^{\nu}b_{\nu}(\beta\cos\vartheta)\mathrm{e}^{\mathrm{j}\nu\varphi} \tag{34}$$

$$E_{\varphi}(r,\vartheta,\varphi) = -2\beta\frac{\mathrm{e}^{-\mathrm{j}\beta r}}{r}\sin\vartheta\sum_{\nu=-\infty}^{\infty}\mathrm{j}^{\nu}a_{\nu}(\beta\cos\vartheta)\mathrm{e}^{\mathrm{j}\nu\varphi} \tag{35}$$

It is worth noting that the summations in the above equations can be efficiently performed via the FFT.

The use of the FFT for the efficient evaluation of the two-dimensional Fourier transforms in Eqs. 31 and 32 is now briefly described. As regards the integration with respect to φ, by a straightforward approximation, it results

$$F_{\nu} = \int_{0}^{2\pi} f(\varphi)\mathrm{e}^{-\mathrm{j}\nu\varphi}\mathrm{d}\varphi \approx \frac{2\pi}{N}\sum_{m=0}^{N-1} f\left(\frac{2\pi m}{N}\right)\mathrm{e}^{-\mathrm{j}2\pi\nu m/N} \tag{36}$$

where $N = 2M_1$, $M_1 = \pi/\Delta\varphi$ is the highest order v of the angular harmonics. Accordingly, save for the factor $2\pi/N$, such an integration can be efficiently performed via a direct FFT algorithm. The integration over z can be tackled in the same way as that along x or y of the plane-rectangular case. Accordingly, by taking into account the truncation due to the finite height $2h$ of the measurement cylinder, it results

$$G(\eta_i) = G\left(\frac{2\pi i}{N_1\Delta z}\right) \approx \frac{2h}{N_1}\mathrm{e}^{-\mathrm{j}\pi i}\sum_{n=0}^{N_1-1} g(z_n)\mathrm{e}^{\mathrm{j}2\pi ni/N_1} \tag{37}$$

where $N_1 = 2h/\Delta z$ is the number of the measurement rings. Thus, the integration over z can be efficiently performed via an inverse FFT algorithm, provided that the so obtained results are multiplied by the factor $2h\mathrm{e}^{-\mathrm{j}\pi i}$.

By summing up, the two-dimensional Fourier transforms of the tangential components of the electric field can be efficiently computed through the following steps: (i) on each measurement ring, the NF data are directly transformed via FFT and then multiplied by the factor 2π/N; (ii) for each index v, the so obtained data are inversely transformed via FFT and then multiplied by $2h\mathrm{e}^{-\mathrm{j}\pi i}$.

Note that the evaluation of the Fourier transform integrals in Eqs. 31 and 32 via the FFT allows one to get the modal expansion coefficients a_v and b_v and, as a consequence, the FF components, at the values of ϑ given by

$$\vartheta_i = \cos^{-1}(\eta_i/\beta) = \cos^{-1}(i\lambda/(N_1\Delta z)) \tag{38}$$

To obtain the FF components with a greater resolution in ϑ, it is sufficient "zero-filling" the NF data. Namely, to get the FF components at the values $\vartheta_i = \cos^{-1}(i\lambda/(N_2\Delta z))$, the NF data must be increased with a proper number of zeros corresponding to fictitious $(N_2 - N_1)/2$ rings at both the ends of the scanning cylinder. In a similar way, to obtain the FF components at $2M_2$ values of φ, the positive and negative angular harmonics must be both augmented with $M_2 - M_1$ zeros before performing the summations in Eqs. 34 and 35 via the FFT.

Since the height of the scanning cylinder is obviously finite, an inevitable truncation error occurs, whose amount depends on the level of the neglected NF data. The angular region wherein the recovered FF pattern is accurate can be determined as in the plane-rectangular case. The truncation error arising when the scanning along φ does not cover a whole 2π range can be handled (Francis 2012) as that occurring in a truncated spherical scan (Hald et al. 1988).

It can be easily recognized that the NF tangential components E_z and E_φ cannot be acquired when performing the measurement by means of a real probe. In fact, it sees the AUT center under different directions when moving on the cylinder. Moreover, also at a fixed position, the probe sees each portion of the AUT under a different direction. As a consequence, the antenna far field cannot be accurately recovered from the measured NF data by employing the uncompensated NF-FF transformation.

The basic theory of probe-compensated NF measurements over a cylinder was developed by Leach and Paris (1973) and is based on an application of the Lorentz reciprocity theorem. They demonstrated rigorously that the modal coefficients a_ν and b_ν of the cylindrical wave expansion of the field radiated by the AUT are related to (i) the two-dimensional Fourier transform of the probe voltage for two independent sets of measurements (the probe is rotated 90° about its longitudinal axis in the second set); (ii) the coefficients of the cylindrical wave expansion of the field radiated by the probe and the rotated probe, when used as transmitting antennas. The key relations to obtain the modal expansion coefficients are

$$a_\nu(\eta) = \frac{\beta^2}{\Lambda^2 \Delta_\nu(\eta)} \left[I_\nu(\eta) \sum_{m=-\infty}^{\infty} d'_m(-\eta) H^{(2)}_{\nu+m}(\Lambda d) - I'_\nu(\eta) \sum_{m=-\infty}^{\infty} d_m(-\eta) H^{(2)}_{\nu+m}(\Lambda d) \right] \tag{39}$$

$$b_\nu(\eta) = \frac{\beta^2}{\Lambda^2 \Delta_\nu(\eta)} \left[I'_\nu(\eta) \sum_{m=-\infty}^{\infty} c_m(-\eta) H^{(2)}_{\nu+m}(\Lambda d) - I_\nu(\eta) \sum_{m=-\infty}^{\infty} c'_m(-\eta) H^{(2)}_{\nu+m}(\Lambda d) \right] \tag{40}$$

$$I_\nu(\eta) = \int_{-\infty}^{\infty} \int_{-\pi}^{\pi} V(\varphi, z)\ \mathrm{e}^{-\mathrm{j}\nu\varphi} \mathrm{e}^{\mathrm{j}\eta z} \mathrm{d}\varphi \mathrm{d}z; \quad I'_\nu(\eta) = \int_{-\infty}^{\infty} \int_{-\pi}^{\pi} V'(\varphi, z)\ \mathrm{e}^{-\mathrm{j}\nu\varphi} \mathrm{e}^{\mathrm{j}\eta z} \mathrm{d}\varphi \mathrm{d}z \tag{41}$$

$$\Delta_\nu(\eta) = \sum_{m=-\infty}^{\infty} c_m(-\eta)H_{\nu+m}^{(2)}(\Lambda d) \sum_{m=-\infty}^{\infty} d'_m(-\eta)H_{\nu+m}^{(2)}(\Lambda d) + \\ - \sum_{m=-\infty}^{\infty} c'_m(-\eta)H_{\nu+m}^{(2)}(\Lambda d) \sum_{m=-\infty}^{\infty} d_m(-\eta)H_{\nu+m}^{(2)}(\Lambda d) \tag{42}$$

where V and V' are the voltages measured by the probe and the rotated probe at the point (d, φ, z). Quite analogous results have been obtained (Yaghjian 1977) by using the source scattering matrix formulation. In fact, as shown in (Appel-Hansen 1980), this last formulation leads, except for a normalization constant, to the same expressions.

The integrals I_ν and I'_ν are again efficiently evaluated via FFT and the NF data are spaced according to Eq. 33. The modal coefficients of the probe (c_m, d_m) and the rotated probe (c'_m, d'_m) can be evaluated from the measured amplitude and phase of the FF components radiated by them (Leach and Paris 1973). Once a_ν and b_ν have been determined, the FF components of the electric field in the spherical coordinate system (r, ϑ, φ) can be evaluated by means of Eqs. 34 and 35.

NF-FF Transformation with Spherical Scanning

The NF-FF transformation with spherical scanning (see Fig. 8) gives the full antenna pattern coverage, even though the data processing is considerably more complicated than that required by planar and cylindrical NF facilities. A tangible amount of work has been done in the past years for formulating and solving the problem of the FF reconstruction from the NF data acquired on a spherical scanning surface (Hald et al. 1988; Wacker 1975; Larsen 1980; Yaghjian and Wittmann 1985). In this framework, a comprehensive book (Hald et al. 1988), which deals with the theoretical as well as the practical aspects of the spherical NF scanning, was published by J.E. Hansen.

There are several ways to perform the scanning in a spherical NF facility (Hald et al. 1988). The most commonly adopted one is the roll-over-azimuth configuration (see Figs. 15 and 16). In such a configuration, the probe stays fixed, whereas the AUT is mounted on a roll positioner (φ axis), which is anchored by means of an L-shaped bracket to an azimuth rotating table (ϑ axis). In the elevation-over-azimuth configuration, the probe stays fixed and the AUT is mounted on an elevation positioner (φ axis), which is mounted on an azimuth rotating table (ϑ axis). On the contrary, in the azimuth-over-elevation setup, the AUT is anchored to an azimuth rotator (φ axis), mounted on an elevation positioner (ϑ axis). Another possibility is to mount the AUT on an azimuth rotating table for selecting the scanning meridian and to move the probe along an arc to perform the scanning along it.

Whatever the configuration has been chosen, the probe can acquire the NF amplitude and phase data on the wanted spherical grid. From these data, measured for two different orientations of the probe and accounting for the probe effects, the

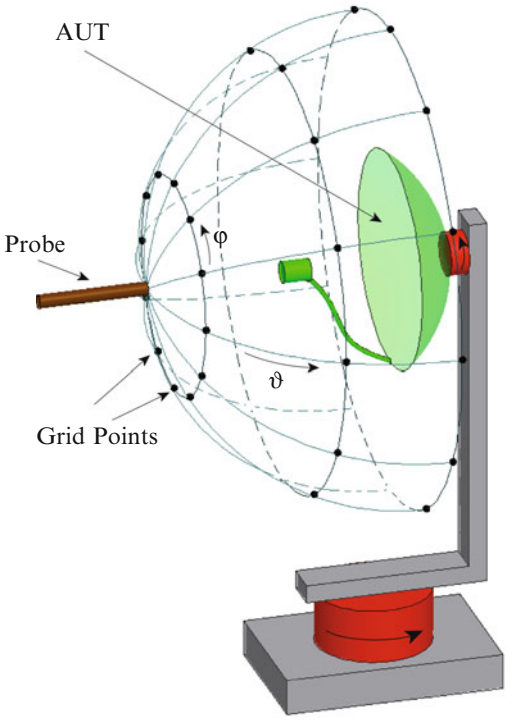

Fig. 15 Roll-over-azimuth NF spherical facility

FF pattern can be evaluated (Hald et al. 1988). As done in the plane-rectangular and cylindrical scanning cases, probe-uncorrected NF-FF transformation formulas, valid in the ideal probe assumption, are initially derived. Then, such an assumption is removed and probe-compensated formulas given.

As well known, in the spherical coordinate system (r, ϑ, φ), the transverse electric field radiated by an AUT can be expressed on a sphere of radius $r = d$ containing it as a superposition of elementary spherical waves (see paragraph "Spherical Wave Expansion"), namely,

$$\underline{E}_t(d,\vartheta,\varphi) = \beta \sum_{n=1}^{N_{\max}} \sum_{m=-n}^{n} \left[a_{1nm} g_{1n}(\beta d) \underline{F}_{1nm}(\vartheta,\varphi) + a_{2nm} g_{2n}(\beta d) \underline{F}_{2nm}(\vartheta,\varphi) \right] \quad (43)$$

where a_{1nm}, a_{2nm} are the spherical wave expansion coefficients,

$$\underline{F}_{1nm}(\vartheta,\varphi) = \underline{f}_{1nm}(\vartheta) \mathrm{e}^{\mathrm{j}m\varphi};\ \underline{F}_{2nm}(\vartheta,\varphi) = \underline{f}_{2nm}(\vartheta) \mathrm{e}^{\mathrm{j}m\varphi} \quad (44)$$

$$\underline{f}_{1nm}(\vartheta) = \left(\frac{-m}{|m|}\right)^m \frac{1}{\sqrt{2\pi n(n+1)}} \left[\frac{\mathrm{j}m}{\sin\vartheta} \overline{P}_n^{|m|}(\cos\vartheta)\hat{\vartheta} - \frac{\mathrm{d}}{\mathrm{d}\vartheta} \overline{P}_n^{|m|}(\cos\vartheta)\hat{\varphi} \right] \quad (45)$$

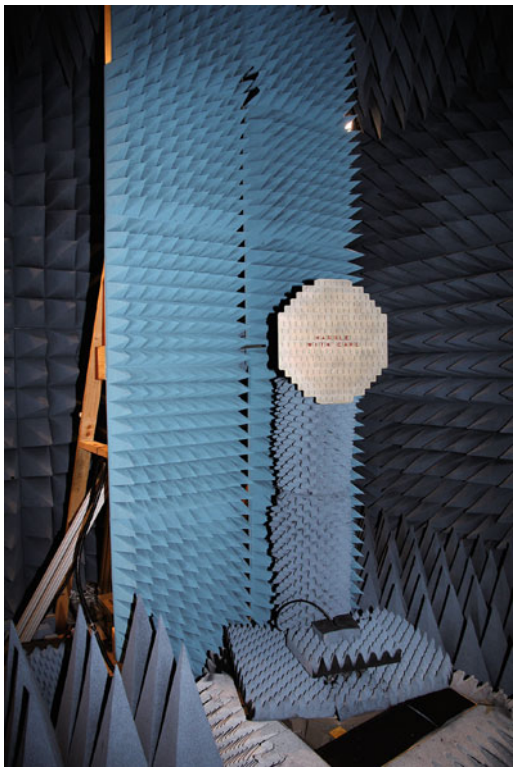

Fig. 16 Photo of the versatile NF system at the UNISA antenna characterization LAB: roll-over-azimuth spherical setup

$$\underline{f}_{2nm}(\vartheta) = \left(\frac{-m}{|m|}\right)^{m} \frac{1}{\sqrt{2\pi n(n+1)}} \left[\frac{\mathrm{d}}{\mathrm{d}\vartheta}\overline{P}_n^{|m|}(\cos\vartheta)\hat{\vartheta} + \frac{\mathrm{j}m}{\sin\vartheta}\overline{P}_n^{|m|}(\cos\vartheta)\hat{\varphi}\right] \tag{46}$$

$$g_{1n}(\beta d) = h_n^{(2)}(\beta d); \quad g_{2n}(\beta d) = \frac{1}{\beta d}\frac{\mathrm{d}}{\mathrm{d}(\beta r)}\left(\beta r h_n^{(2)}(\beta r)\right)\Big|_{r=d} \tag{47}$$

$h_n^{(2)}(x)$ being the spherical Hankel function of second kind and order n.

In the classical approach (Hald et al. 1988), the choice of the highest spherical wave is usually determined according to the following rule of thumb:

$$N_{\max} = \mathrm{Int}(\beta a) + 10 \tag{48}$$

where a is the radius of the smallest sphere enclosing the AUT. In the approach (Bucci et al. 2001a), it is rigorously fixed by the spatial band limitation properties of the radiated EM fields (Bucci and Franceschetti 1987) and it results

$$N_{\max} = \mathrm{Int}(\chi'\beta a) + 1 \tag{49}$$

where χ' is an enlargement bandwidth factor slightly larger than unity for electrically large antennas (Bucci and Franceschetti 1987).

In Eqs. 45 and 46, $\overline{P}_n^{|m|}(x)$ (see Eq. 107) is the normalized associated Legendre function as defined by Belousov (1962).

The expansion coefficients a_{1nm}, a_{2nm} can be evaluated from the knowledge of the tangential electric field on the scanning sphere by taking into account that the spherical vector wave functions $\underline{F}_{1,2nm}(\vartheta,\varphi)$ are orthonormal. As a matter of fact, from Eq. 43 it results

$$\left\langle \underline{E}_t, \underline{F}_{1,2nm} \right\rangle = \int_0^{2\pi}\int_0^{\pi} \underline{E}_t(d,\vartheta,\varphi)\cdot \underline{F}^*_{1,2nm}(\vartheta,\varphi)\sin\vartheta \mathrm{d}\vartheta\mathrm{d}\varphi = \beta a_{1,2nm}\, g_{1,2n}(\beta d) \quad (50)$$

where the asterisk (*) indicates the complex conjugation, and therefore

$$a_{1,2nm} = \frac{1}{\beta g_{1,2n}(\beta d)} \int_0^{2\pi}\int_0^{\pi} \underline{E}_t(d,\vartheta,\varphi)\cdot \underline{f}^*_{1,2nm}(\vartheta)\mathrm{e}^{-\mathrm{j}m\varphi}\sin\vartheta \mathrm{d}\vartheta d\varphi \quad (51)$$

Once the spherical wave expansion coefficients have been determined, the transverse electric field radiated by the AUT in the FF region can be evaluated (see paragraph "Spherical Wave Expansion") by the FF spherical wave expansion:

$$\underline{E}_t(r,\vartheta,\varphi) = \frac{\mathrm{e}^{-\mathrm{j}\beta r}}{r}\sum_{n=1}^{N_{\max}}\sum_{m=-n}^{n}\left[\mathrm{j}^{n+1}a_{1nm}\underline{f}_{1nm}(\vartheta) + \mathrm{j}^n a_{2nm}\underline{f}_{2nm}(\vartheta)\right]\mathrm{e}^{\mathrm{j}m\varphi} \quad (52)$$

As will be shown in the following, the FFT is used to evaluate the modal coefficients in an efficient way, and the sample spacings of the NF data in the classical approach (Hald et al. 1988) are

$$\Delta\vartheta \leqslant 2\pi/(2N_{\max}+1); \quad \Delta\varphi = \Delta\vartheta \quad (53)$$

The number of NF data along φ can be reduced if the radius a' of the smallest cylinder enclosing the AUT and having its axis coincident with the z one is smaller than the radius a of the minimum sphere. In such a case, it results (Hald et al. 1988)

$$\Delta\varphi \leqslant 2\pi/(2M+1) \quad (54)$$

where $M = \mathrm{Int}\,(\beta a') + 10$.

In the approach (Bucci et al. 2001a), the sample spacings are rigorously fixed by the spatial band limitation properties of the radiated EM fields (Bucci and Franceschetti 1987) and, accordingly, $N_{\max}$ is now given by Eq. 49, whereas $\Delta\varphi$ is given by Eq. 54, where M decreases when moving from the sampling parallels near the equator to those near the poles according to the law

$$M = \mathrm{Int}(\chi^* \beta a \sin\vartheta) + 1 \tag{55}$$

In this last relation,

$$\chi^* = \chi^*(\vartheta) = 1 + (\chi' - 1)[\sin\vartheta]^{-2/3} \tag{56}$$

is the azimuthal enlargement bandwidth factor.

The efficient evaluation of Eq. 51 is now briefly described. By expanding the tangential electric field components on the measurement sphere in Fourier series with respect to φ, namely,

$$\underline{E}_t(d, \vartheta, \varphi) = \sum_{k=-M}^{M} \underline{G}_k(\vartheta) \mathrm{e}^{\mathrm{j}k\varphi} \tag{57}$$

the coefficients can be rewritten as follows:

$$a_{1,2nm} = \frac{2\pi}{\beta g_{1,2n}(\beta d)} \int_0^{\pi} \underline{G}_m(\vartheta) \cdot \underline{f}^*_{-1,2nm}(\vartheta) \sin\vartheta \mathrm{d}\vartheta \tag{58}$$

The integration over ϑ in Eq. 58 can be efficiently carried out by expanding in Fourier series the components of $\underline{G}_m(\vartheta)$ and $\underline{f}_{-1,2nm}(\vartheta)$ via FFT. Accordingly, it results

$$a_{1,2nm} = \frac{2\pi}{\beta g_{1,2n}(\beta d)} \sum_{\ell=-N_{\max}}^{N_{\max}} \sum_{i=-N_{\max}}^{N_{\max}} \underline{G}_{m\ell} \cdot \underline{f}^*_{-1,2nmi} \int_0^{\pi} \mathrm{e}^{\mathrm{j}(\ell-i)\vartheta} \sin\vartheta \, \mathrm{d}\vartheta \tag{59}$$

The integral in Eq. 58 is so transformed in a double summation, of indexes ℓ and i, involving the Fourier series coefficients (in ϑ) of the components of $\underline{G}_m(\vartheta)$ and $\underline{f}_{-1,2nm}(\vartheta)$, and the integrals

$$\int_0^{\pi} \mathrm{e}^{\mathrm{j}(\ell-i)\vartheta} \sin\vartheta \mathrm{d}\vartheta$$

Note that, in order to evaluate the Fourier series coefficients of the components of $\underline{G}_m(\vartheta)$ and $\underline{f}_{-1,2nm}(\vartheta)$, it is necessary to extend the components of $\underline{G}_m(\vartheta)$ and $\underline{f}_{-1,2nm}(\vartheta)$, from $[0, \pi]$ on the range $[0, 2\pi]$. This can be easily done by taking into account that (i) the components of $\underline{f}_{-1,2nm}(\vartheta)$ are even about $\vartheta = \pi$ when m is odd, and vice versa; (ii) the components of $\underline{G}_m(\vartheta)$ have the same parity as those of $\underline{f}_{-1,2nm}(\vartheta)$.

To take advantage of the numerical efficiency of the standard FFT algorithm, the number of NF parallels to be considered in the NF-FF transformation and the number of samples on them must be the first power of two greater or equal to $N_{\max}$ and $2M$, respectively.

Moreover, by inverting the summation order in Eq. 52, it can be rewritten in the form

$$\underline{E}_t(r,\vartheta,\varphi) = \frac{\mathrm{e}^{-\mathrm{j}\beta r}}{r} \sum_{m=-M}^{M} \sum_{\substack{n=|m| \\ (n\neq 0)}}^{N_{\max}} \left[\mathrm{j}^{n+1} a_{1nm} \underline{f}_{1nm}(\vartheta) + \mathrm{j}^{n} a_{2nm} \underline{f}_{2nm}(\vartheta)\right] \mathrm{e}^{\mathrm{j}m\varphi} \tag{60}$$

which allows an efficient evaluation of the antenna far field at the considered elevation angle ϑ by performing the summation via FFT.

It can be easily recognized that the NF tangential components E_ϑ and E_φ cannot be acquired when performing the measurement with a real probe. In fact, it sees each portion of the AUT under a different direction. As a consequence, the antenna far field cannot be accurately recovered from the measured NF data by using the uncompensated NF-FF transformation.

The probe-compensated NF-FF transformation with spherical scanning has been developed by using the source scattering matrix formulation. As shown in (Hald et al. 1988), when using a probe with a first-order azimuthal dependence FF pattern (e.g., an open-ended circular waveguide), the modal expansion coefficients can be determined from the knowledge of the voltages V and V' measured by the probe and rotated probe, respectively, and are given by

$$a_{1nm} = \frac{2n+1}{16\pi} \frac{\int_0^{\pi}\int_0^{2\pi} [I_1(\vartheta)V - \mathrm{j}\, I_2(\vartheta)V']\mathrm{e}^{-\mathrm{j}m\varphi} \sin\vartheta \;\mathrm{d}\varphi\,\mathrm{d}\vartheta}{\sum_{v=1}^{v_{\max}} \left[a'_{1v1} A^n_{v1}(\beta d) - a'_{2v1} B^n_{v1}(\beta d)\right]} \tag{61}$$

$$a_{2nm} = \frac{2n+1}{16\pi} \frac{\int_0^{\pi}\int_0^{2\pi} [I_2(\vartheta)V - \mathrm{j}\; I_1(\vartheta)V']\mathrm{e}^{-\mathrm{j}m\varphi} \sin\vartheta \;\mathrm{d}\varphi\,\mathrm{d}\vartheta}{\sum_{v=1}^{v_{\max}} \left[a'_{1v1} B^n_{v1}(\beta d) - a'_{2v1} A^n_{v1}(\beta d)\right]} \tag{62}$$

where $v_{\max}$ is the highest spherical wave of the probe, $a'_{1,2v1}$ are its expansion coefficients,

$$I_1(\vartheta) = \left[d^n_{1m}(\vartheta) - d^n_{-1m}(\vartheta)\right]; \quad I_2(\vartheta) = \left[d^n_{1m}(\vartheta) + d^n_{-1m}(\vartheta)\right] \tag{63}$$

and

$$d^n_{\mu m}(\vartheta) = \sqrt{\frac{(n+\mu)!(n-\mu)!}{(n+m)!(n-m)!}} \sum_{\sigma} \binom{n+m}{n-\mu-\sigma} \binom{n-m}{\sigma} (-1)^{n-\mu-\sigma} \cdot \left(\cos\tfrac{\vartheta}{2}\right)^{2\sigma+\mu+m} \left(\sin\tfrac{\vartheta}{2}\right)^{2n-2\sigma-\mu-m} \tag{64}$$

are the rotation coefficients (Hald et al. 1988; Edmonds 1974), the summation over σ involving all terms in which the binomial coefficients do not lead to negative arguments for the factorials. Moreover,

$$A^n_{\nu\mu}(\beta d) = \sqrt{\frac{(2n+1)(2\nu+1)}{n(n+1)\nu(\nu+1)}}\sqrt{\frac{(\nu+\mu)!(n-\mu)!}{(\nu-\mu)!(n+\mu)!}}(-1)^{\mu}\frac{1}{2}\mathrm{j}^{n-\nu}\cdot \cdot \sum_{p=|n-\nu|}^{n+\nu}\left\{\mathrm{j}^{-p}[n(n+1)+\nu(\nu+1)-p(p+1)]\tau(\mu,n,-\mu,\nu,p)h^{(2)}_p(\beta d)\right\} \tag{65}$$

$$B^n_{\nu\mu}(\beta d) = \sqrt{\frac{(2n+1)(2\nu+1)}{n(n+1)\nu(\nu+1)}}\sqrt{\frac{(\nu+\mu)!(n-\mu)!}{(\nu-\mu)!(n+\mu)!}}(-1)^{\mu}\frac{1}{2}\mathrm{j}^{n-\nu}\cdot \cdot \sum_{p=|n-\nu|}^{n+\nu}\left[\mathrm{j}^{-p}(2\mathrm{j}\mu\beta d)\,\tau(\mu,n,-\mu,\nu,p)\,h^{(2)}_p(\beta d)\right] \tag{66}$$

are the translation coefficients (Hald et al. 1988; Larsen 1980; Bruning and Lo 1971), wherein $\tau(\mu, n, -\mu, \nu, p)$ are the linearization coefficients defined by the expansion of the product of two unnormalized associated Legendre functions

$$P^{\mu}_n(x)P^{-\mu}_{\nu}(x) = \sum_{p=|n-\nu|}^{n+\nu}\tau(\mu,n,-\mu,\nu,p)P_p(x) \tag{67}$$

The probe expansion coefficients $a'_{1,2\nu1}$ in Eqs. 61, 62 can be evaluated from the knowledge of its tangential electric field $\underline{E}'_t$ on a scanning sphere when it is used as transmitting antenna

$$a'_{1,2\nu1} = \frac{1}{\beta g_{1,2\nu}(\beta d)}\int_0^{2\pi}\int_0^{\pi}\underline{E}'_t(d,\vartheta,\varphi)\cdot\underline{f}^{*}_{1,2\nu1}(\vartheta)\mathrm{e}^{-\mathrm{j}\varphi}\sin\vartheta\,\mathrm{d}\vartheta\,\mathrm{d}\varphi \tag{68}$$

Classical Wave Expansions of the Field Radiated by an Antenna

Some analytical details on the wave expansions commonly employed to represent the antenna field in the region external to it are collected in this paragraph. In any case, its reading is not strictly necessary for the comprehension of the chapter and its aim is to enable the interested reader to achieve a more in-depth knowledge of the topic.

Plane Wave Expansion

As well known, in a linear, homogeneous, and isotropic medium, an EM field

$$\underline{\mathbf{E}} = \underline{\mathbf{E}}\mathrm{e}^{-\mathrm{j}\underline{k}\cdot\underline{r}};\ \underline{\mathbf{H}} = \underline{\mathbf{H}}\mathrm{e}^{-\mathrm{j}\underline{k}\cdot\underline{r}} \tag{69}$$

represents a time-harmonic plane wave whose direction of propagation is specified by the vector $\underline{\mathbf{k}} = k_x\mathbf{x} + k_y\mathbf{y} + k_z\mathbf{z}$.

Since the operator ∇ transforms into $-\mathrm{j}\underline{k}$ for such a field, Maxwell's equations in a region free of sources become

$$\underline{\mathbf{k}} \times \underline{\mathbf{E}} = \omega\mu\underline{\mathbf{H}} \tag{70}$$

$$\underline{\mathbf{k}} \times \underline{\mathbf{H}} = -\omega\varepsilon\underline{\mathbf{E}} \tag{71}$$

$$\underline{\mathbf{k}} \cdot \underline{\mathbf{E}} = 0 \tag{72}$$

$$\underline{\mathbf{k}} \cdot \underline{\mathbf{H}} = 0 \tag{73}$$

From Eqs. 70 and 71, it results that $\underline{\mathbf{E}}$ and $\underline{\mathbf{H}}$ cannot be chosen independently, for instance, $\underline{\mathbf{H}}$ is related to $\underline{\mathbf{E}}$ by

$$\underline{\mathbf{H}} = \frac{1}{\omega\mu}\underline{\mathbf{k}} \times \underline{\mathbf{E}} \tag{74}$$

From Eq. 72, it results that, for any k_x, k_y, and k_z, only two components of $\underline{\mathbf{E}}(\underline{\mathbf{k}})$ are independent. Let these be $\mathbf{E}_x$ and $\mathbf{E}_y$, then

$$\mathbf{E}_z = -\left(\mathbf{E}_x k_x + \mathbf{E}_y k_y\right)/k_z \tag{75}$$

From Eq. 70, it results that

$$\underline{\mathbf{k}} \times (\underline{\mathbf{k}} \times \underline{\mathbf{E}}) = \omega\mu\underline{\mathbf{k}} \times \underline{\mathbf{H}} \tag{76}$$

Such a relation, taking into account Eqs. 71, 72 and the vector identity $\underline{\mathbf{a}} \times (\underline{\mathbf{b}} \times \underline{\mathbf{c}}) = \underline{\mathbf{b}}(\underline{\mathbf{a}} \cdot \underline{\mathbf{c}}) - \underline{\mathbf{c}}(\underline{\mathbf{a}} \cdot \underline{\mathbf{b}})$, becomes

$$\underline{\mathbf{E}}\left[(\underline{\mathbf{k}} \cdot \underline{\mathbf{k}}) - \omega^2\varepsilon\mu\right] = 0 \tag{77}$$

In order that such an equation have a solution different from the trivial one $\underline{\mathbf{E}} = 0$, it is necessary that

$$\underline{\mathbf{k}} \cdot \underline{\mathbf{k}} = k_x^2 + k_y^2 + k_z^2 = \omega^2\varepsilon\mu = \beta^2 \tag{78}$$

Thus, at a fixed frequency, only two of the components of $\underline{\mathbf{k}}$ can be independently specified. Let these be k_x and k_y, then the third component is related to them via the relation

$$k_z = \begin{cases} \left(\beta^2 - k_x^2 - k_y^2\right)^{1/2}, & \text{if } k_x^2 + k_y^2 \leqslant \beta^2 \\ -\mathrm{j}\left(k_x^2 + k_y^2 - \beta^2\right)^{1/2}, & \text{if } k_x^2 + k_y^2 > \beta^2 \end{cases} \tag{79}$$

The negative sign in the second of Eq. 79 is chosen in order to ensure that the plane wave Eq. 69 is bounded at infinity.

Since the medium is linear as well as the field equations, the general solution for $\underline{\mathbf{E}}$ and $\underline{\mathbf{H}}$ can be constructed as linear combination over all k_x and k_y:

$$\underline{E}(\underline{r}) = \int_{-\infty}^{+\infty}\int_{-\infty}^{+\infty} \underline{\mathbf{E}}(\underline{k})\mathrm{e}^{-\mathrm{j}\underline{k}\cdot\underline{r}}\,\mathrm{d}k_x\mathrm{d}k_y;\ \underline{H}(\underline{r}) = \int_{-\infty}^{+\infty}\int_{-\infty}^{+\infty} \frac{1}{\omega\mu}\underline{k}\times\underline{\mathbf{E}}(\underline{k})\mathrm{e}^{-\mathrm{j}\underline{k}\cdot\underline{r}}\,\mathrm{d}k_x\mathrm{d}k_y \quad (80)$$

Namely, any arbitrary monochromatic wave can be represented as a superposition of plane waves with different amplitudes and propagating in different directions. The amplitude function $\underline{\mathbf{E}}(\underline{k})$ is called the plane wave spectrum of the field. It is worthy to note that the dimensions of $\underline{\mathbf{E}}$ in Eqs. 69 and 80 are different although the same notation has been used.

In general, the evaluation of the double integral in Eq. 80 is difficult. However, it can be shown (Franceschetti 1997; Balanis 1997), by applying the stationary phase method, that in the far-field region such an integral can be represented by the asymptotic expansion

$$\underline{\mathbf{E}}(r,\vartheta,\varphi) = \mathrm{j}2\pi k_z\underline{\mathbf{E}}\left(k_x,k_y\right)\frac{\mathrm{e}^{-\mathrm{j}\beta r}}{r} \quad (81)$$

where

$$k_x = \beta\sin\vartheta\cos\varphi;\quad k_y = \beta\sin\vartheta\sin\varphi;\quad k_z = \beta\cos\vartheta \quad (82)$$

Cylindrical Wave Expansion

In the cylindrical wave expansion (CWE), the field is represented as superposition of transverse electric (TE) and transverse magnetic (TM) cylindrical modes (Stratton 1941), which are elementary solutions of the homogeneous wave equation in the cylindrical coordinates (ρ, φ, z). In fact, an arbitrary field in a homogeneous source-free region can be always expressed as the sum of a TE field and a TM field (Harrington 1961). The expression for these modes can be easily derived by using the auxiliary vector potentials $\underline{\mathbf{A}}$ and $\underline{\mathbf{F}}$, which, in such a hypothesis, are solutions of the homogeneous vector Helmoltz equations:

$$\nabla^2\underline{\mathbf{A}} + \beta^2\underline{\mathbf{A}} = 0;\ \nabla^2\underline{\mathbf{F}} + \beta^2\underline{\mathbf{F}} = 0 \quad (83)$$

As well known, the fields $\underline{\mathbf{E}}$ and $\underline{\mathbf{H}}$ are related to them by

$$\underline{\mathbf{E}} = -\mathrm{j}\omega\underline{\mathbf{A}} + \frac{\nabla\nabla\cdot\underline{\mathbf{A}}}{\mathrm{j}\omega\varepsilon\mu} - \frac{1}{\varepsilon}\nabla\times\underline{\mathbf{F}};\quad \underline{\mathbf{H}} = -\mathrm{j}\omega\underline{\mathbf{F}} + \frac{\nabla\nabla\cdot\underline{\mathbf{F}}}{\mathrm{j}\omega\varepsilon\mu} + \frac{1}{\mu}\nabla\times\underline{\mathbf{A}} \quad (84)$$

From Eq. 84, it can be easily recognized that, to derive the field expressions that are TE to z, it is sufficient to assume (Balanis 1989)

$$\underline{\mathbf{A}} = 0;\ \underline{\mathbf{F}} = \mathbf{z}\mathbf{F}(\rho, \varphi, z) \tag{85}$$

whereas

$$\underline{\mathbf{A}} = \mathbf{z}\mathbf{A}(\rho, \varphi, z);\ \underline{\mathbf{F}} = 0 \tag{86}$$

for the TM to z modes (Balanis 1989). In both the cases, the vector Helmoltz equations reduce to the scalar ones. Their elementary solution is obtainable by using the separation of variables method (Balanis 1989) and, in the considered case of observation region external to smallest cylinder enclosing the AUT, is given by $H_{\nu}^{(2)}(\Lambda\rho)\mathrm{e}^{\mathrm{j}\nu\varphi}\mathrm{e}^{-\mathrm{j}\eta z}$, where ν is an integer, η is a real number, $\Lambda = \left(\beta^2 - \eta^2\right)^{1/2}$, and $H_{\nu}^{(2)}(\Lambda\rho)$ is the Hankel function of second kind and order ν.

By substituting such an elementary solution in Eq. 84, it results

$$\underline{\mathbf{E}} = (-1/\varepsilon)\underline{\mathbf{M}}_{\nu\eta} \tag{87}$$

for the TE case and

$$\underline{\mathbf{E}} = (\beta/\mathrm{j}\omega\varepsilon\mu)\underline{\mathbf{N}}_{\nu\eta} \tag{88}$$

for the TM one, wherein

$$\underline{\mathbf{M}}_{\nu\eta}(\rho, \varphi, z) = \left(\frac{\mathrm{j}\nu}{\rho}H_{\nu}^{(2)}(\Lambda\rho)\hat{\rho} - \frac{\partial}{\partial\rho}H_{\nu}^{(2)}(\Lambda\rho)\hat{\varphi}\right)\mathrm{e}^{\mathrm{j}\nu\varphi}\mathrm{e}^{-\mathrm{j}\eta z} \tag{89}$$

$$\underline{\mathbf{N}}_{\nu\eta}(\rho, \varphi, z) = \left(-\frac{\mathrm{j}\eta}{\beta}\frac{\partial}{\partial\rho}H_{\nu}^{(2)}(\Lambda\rho)\hat{\rho} + \frac{\nu\eta}{\beta\rho}H_{\nu}^{(2)}(\Lambda\rho)\hat{\varphi} + \frac{\Lambda^2}{\beta}H_{\nu}^{(2)}(\Lambda\rho)\hat{z}\right)\mathrm{e}^{\mathrm{j}\nu\varphi}\mathrm{e}^{-\mathrm{j}\eta z} \tag{90}$$

Accordingly, the electric field radiated by the AUT at a point external to the smallest cylinder enclosing it can be represented (Stratton 1941) as a linear combination of the elementary fields Eqs. 87 and 88 involving an integral over all η values, and a sum over all ν:

$$\underline{\mathbf{E}}(\rho, \varphi, z) = \sum_{\nu=-\infty}^{\infty}\int_{-\infty}^{\infty}\left[a_{\nu}(\eta)\underline{\mathbf{M}}_{\nu\eta}(\rho, \varphi, z) + b_{\eta}(\eta)\underline{\mathbf{N}}_{\nu\eta}(\rho, \varphi, z)\right]\mathrm{d}\eta \tag{91}$$

therefore

$$E_{\rho}(\rho, \varphi, z) = \sum_{\nu=-\infty}^{\infty}\int_{-\infty}^{\infty}\left[a_{\nu}(\eta)\frac{\mathrm{j}\nu}{\rho}H_{\nu}^{(2)}(\Lambda\rho) - \frac{\mathrm{j}\eta}{\beta}b_{\nu}(\eta)\frac{\partial}{\partial\rho}H_{\nu}^{(2)}(\Lambda\rho)\right]\mathrm{e}^{\mathrm{j}\nu\varphi}\mathrm{e}^{-\mathrm{j}\eta z}\mathrm{d}\eta \tag{92}$$

$$E_\varphi(\rho,\varphi,z)=\sum_{\nu=-\infty}^{\infty}\int_{-\infty}^{\infty}\left[b_\nu(\eta)\frac{\nu\eta}{\beta\rho}H_\nu^{(2)}(\Lambda\rho)-a_\nu(\eta)\frac{\partial}{\partial\rho}H_\nu^{(2)}(\Lambda\rho)\right]\mathrm{e}^{\mathrm{j}\nu\varphi}\mathrm{e}^{-\mathrm{j}\eta z}\mathrm{d}\eta \quad (93)$$

$$E_z(\rho,\varphi,z)=\sum_{\nu=-\infty}^{\infty}\int_{-\infty}^{\infty}b_\nu(\eta)\frac{\Lambda^2}{\beta}H_\nu^{(2)}(\Lambda\rho)\mathrm{e}^{\mathrm{j}\nu\varphi}\mathrm{e}^{-\mathrm{j}\eta z}\mathrm{d}\eta \quad (94)$$

The evaluations of the FF components of the electric field in the spherical coordinate system (r, ϑ, φ) from the above expressions involve the following steps. The first step is to replace in the CWE the Hankel function and its first derivative by their asymptotic expansions

$$H_\nu^{(2)}(x)\underset{x\to\infty}{\approx}\sqrt{\frac{2\mathrm{j}}{\pi x}}\mathrm{j}^\nu\mathrm{e}^{-\mathrm{j}x};\quad \frac{\mathrm{d}}{\mathrm{d}x}H_\nu^{(2)}(\alpha x)\underset{x\to\infty}{\approx}\sqrt{\frac{2\mathrm{j}\alpha}{\pi x}}\mathrm{j}^{\nu-1}\mathrm{e}^{-\mathrm{j}\alpha x} \quad (95)$$

The obtained expressions are then rewritten in terms of the spherical coordinates r, ϑ, φ. The next step is the asymptotic evaluation of the integrals over η by means of the method of the stationary phase (James 1980). At last, the FF components of the electric field in the cylindrical coordinate system are transformed in the spherical ones, thus obtaining Eqs. 34 and 35.

Spherical Wave Expansion

In the spherical wave expansion (SWE), the field is represented as superposition of transverse electric (to the radial direction) spherical modes (TE^r) and transverse magnetic ones (TM^r) (Stratton 1941), which are elementary solutions of the homogeneous wave equation in the spherical coordinates (r, ϑ, φ). In fact, an arbitrary field in a homogeneous source-free region can be expressed as the sum of a TE field and a TM field (Harrington 1961). The expression for these modes can be determined by using the auxiliary vector potentials $\underline{\mathbf{A}}$ and $\underline{\mathbf{F}}$. In particular, to derive the field expressions that are TE to r, it is sufficient to assume (Balanis 1989)

$$\underline{\mathbf{A}}=0;\quad \underline{\mathbf{F}}=\mathbf{r}F(r,\vartheta,\varphi) \quad (96)$$

whereas

$$\underline{\mathbf{A}}=\mathbf{r}A(r,\vartheta,\varphi);\quad \underline{\mathbf{F}}=0 \quad (97)$$

for the TM to r modes (Balanis 1989).

It must be stressed that, unlike the cylindrical scanning case, it is not convenient now to determine the auxiliary potentials by means of the vector Helmholtz equations (Eq. 83), valid in a source-free region when assuming that the vector potentials $\underline{\mathbf{A}}$, $\underline{\mathbf{F}}$ and the scalar ones Φ, Ψ satisfy the Lorentz conditions:

$$\nabla\cdot\underline{\mathbf{A}}+\mathrm{j}\omega\varepsilon\mu\Phi=0;\quad \nabla\cdot\underline{\mathbf{F}}+\mathrm{j}\omega\varepsilon\mu\Psi=0 \quad (98)$$

In fact, since $\nabla^2(\mathbf{r}G) \neq \mathbf{r}\nabla^2 G$, the vector Helmholtz equations (Eq. 83) do not reduce any longer to the corresponding scalar ones. Obviously, in such a case, also the expressions (Eq. 84), relating the fields to the auxiliary potentials, are no longer valid. Different relations for the fields and potentials that are not based on Lorentz conditions are now derived.

The TE^r case $(\underline{\mathbf{A}} = 0, \underline{\mathbf{F}} = \mathbf{r}\mathbf{F}(r, \vartheta, \varphi))$ is first considered. It can be easily recognized that

$$\underline{\mathbf{E}} = -\frac{1}{\varepsilon}\nabla \times \underline{\mathbf{F}}; \quad \underline{\mathbf{H}} = \frac{1}{\mathrm{j}\omega\varepsilon\mu}\nabla \times \nabla \times \underline{\mathbf{F}} \tag{99}$$

By substituting the former of Eq. 99 in the second of Maxwell's equations, it results

$$\nabla \times (\underline{\mathbf{H}} + \mathrm{j}\omega\underline{\mathbf{F}}) = 0 \tag{100}$$

and, accordingly,

$$\underline{\mathbf{H}} = -\mathrm{j}\omega\underline{\mathbf{F}} - \nabla\Psi \tag{101}$$

By substituting Eq. 101 into the latter of Eq. 99, it is obtained

$$\nabla \times \nabla \times \underline{\mathbf{F}} - \beta^2\underline{\mathbf{F}} = -\mathrm{j}\omega\varepsilon\mu\nabla\Psi \tag{102}$$

By expanding Eq. 102 in spherical coordinates and imposing that $\Psi = (-1/\mathrm{j}\omega\varepsilon\mu)$ $\partial F/\partial r$, it can be shown (Balanis 1989) that F can be determined by solving the scalar Helmholtz equation

$$\nabla^2\psi + \beta^2\psi = 0 \tag{103}$$

where

$$\psi(r, \vartheta, \varphi) = F(r, \vartheta, \varphi)/r \tag{104}$$

The elementary solution to Eq. 103 can be obtained by using the separation of variables method (Balanis 1989) and, in the considered case of an observation region external to the smallest sphere enclosing the AUT, it is given by

$$\psi(r, \vartheta, \varphi) = h_n^{(2)}(\beta r)\overline{P}_n^{|m|}(\cos\vartheta)\mathrm{e}^{\mathrm{j}m\varphi} \tag{105}$$

where n and m are integers, $\overline{P}_n^m(x)$ is the normalized associated Legendre function as defined by Belousov (1962), and $h_n^{(2)}(x)$ is the spherical Hankel function of second kind and order n, which is related to the ordinary Hankel function of second kind by

$$h_n^{(2)}(x) = \sqrt{\frac{\pi}{2x}}H_{n+1/2}^{(2)}(x) \tag{106}$$

The normalized associated Legendre function $\overline{P}_n^m(x)$ is related to the associated Legendre function $P_n^m(x)$ (solution of the associated Legendre differential equation (Balanis 1989)) by

$$\overline{P}_n^m(x) = \sqrt{\frac{2n+1}{2}\frac{(n-m)!}{(n+m)!}}P_n^m(x) \tag{107}$$

A similar procedure can be applied in the TM^r case $(\underline{\mathbf{A}} = \mathbf{r}A(r,\vartheta,\varphi), \underline{\mathbf{F}} = 0)$, thus obtaining

$$\underline{\mathbf{H}} = \frac{1}{\mu}\nabla \times \underline{\mathbf{A}};\ \ \underline{\mathbf{E}} = \frac{1}{\mathrm{j}\omega\varepsilon\mu}\nabla \times \nabla \times \underline{\mathbf{A}} \tag{108}$$

and

$$\nabla \times \nabla \times \underline{\mathbf{A}} - \beta^2 \underline{\mathbf{A}} = -\mathrm{j}\omega\varepsilon\mu\nabla\Phi \tag{109}$$

By expanding Eq. 109 in spherical coordinates and imposing that $\Phi = (-1/\mathrm{j}\omega\varepsilon\mu)$ $\partial A/\partial r$, it can be shown (Balanis 1989) that A can be determined by solving the scalar Helmholtz equation (Eq. 103), wherein now

$$\psi(r,\vartheta,\varphi) = A(r,\vartheta,\varphi)/r \tag{110}$$

The transverse electric field $\underline{E}_t$ related to an elementary spherical TE^r wave can be easily found from the former of Eq. 99, by expanding $\nabla \times \underline{\mathbf{F}}$ in spherical coordinates and taking into account Eqs. 104 and 105, thus obtaining

$$\underline{E}_t = -\frac{1}{\varepsilon}g_{1n}(\beta r)\underline{\widetilde{E}}_{1nm}(\vartheta,\varphi) = -\frac{1}{\varepsilon}g_{1n}(\beta r)\underline{\widetilde{f}}_{1nm}(\vartheta)\mathrm{e}^{\mathrm{j}m\varphi} \tag{111}$$

where

$$g_{1n}(\beta r) = h_n^{(2)}(\beta r);\ \ \underline{\widetilde{f}}_{1nm}(\vartheta) = \frac{\mathrm{j}m}{\sin\vartheta}\overline{P}_n^{|m|}(\cos\vartheta)\boldsymbol{\vartheta} - \frac{\mathrm{d}}{\mathrm{d}\vartheta}\overline{P}_n^{|m|}(\cos\vartheta)\boldsymbol{\varphi} \tag{112}$$

In a similar way, the transverse electric field related to an elementary spherical TM^r wave can be determined from the latter of Eq. 108, by expanding $\nabla \times \nabla \times \underline{\mathbf{A}}$ in spherical coordinates and taking into account relations Eqs. 105 and 110, thus getting

$$\underline{E}_t = \frac{\beta}{\mathrm{j}\omega\varepsilon\mu}g_{2n}(\beta r)\underline{\widetilde{F}}_{2nm}(\vartheta,\varphi) = \frac{\beta}{\mathrm{j}\omega\varepsilon\mu}g_{2n}(\beta r)\underline{\widetilde{f}}_{2nm}(\vartheta)\mathrm{e}^{\mathrm{j}m\varphi} \tag{113}$$

where

$$g_{2n}(\beta r) = \frac{1}{\beta r}\frac{\mathrm{d}}{\mathrm{d}(\beta r)}\left(\beta r h_n^{(2)}(\beta r)\right);\ \ \underline{\widetilde{f}}_{2nm}(\vartheta) = \frac{\mathrm{d}}{\mathrm{d}\vartheta}\overline{P}_n^{|m|}(\cos\vartheta)\boldsymbol{\vartheta} + \frac{\mathrm{j}m}{\sin\vartheta}\overline{P}_n^{|m|}(\cos\vartheta)\boldsymbol{\varphi} \tag{114}$$

By expressing the transverse electric field radiated by the AUT on a sphere of radius r containing it as a superposition of elementary TE^r and TM^r spherical waves, it results

$$\underline{E}_t = \sum_{n=1}^{N_{\max}} \sum_{m=-n}^{n} \left[\tilde{a}_{1nm} g_{1n}(\beta r) \widetilde{\underline{F}}_{1nm}(\vartheta, \varphi) + \tilde{a}_{2nm} g_{2n}(\beta r) \widetilde{\underline{F}}_{2nm}(\vartheta, \varphi) \right] \tag{115}$$

where $N_{\max}$ is the index of the highest spherical wave to be considered. It is worth noting that the summation on m extends from $-n$ to n, since $\overline{P}_n^{|m|}(\cos\vartheta)$ vanishes for $|m| > n$, whereas that on n starts from 1, since $\widetilde{\underline{F}}_{100}$ and $\widetilde{\underline{F}}_{200}$ are both null (Hald et al. 1988).

It can be shown (Hald et al. 1988) that

$$\left\langle \widetilde{\underline{F}}_{1nm}, \widetilde{\underline{F}}_{2\overline{n}\overline{m}} \right\rangle = \int_0^{2\pi} \int_0^{\pi} \widetilde{\underline{F}}_{1nm}(\vartheta, \varphi) \cdot \widetilde{\underline{F}}^*_{2\overline{n}\overline{m}}(\vartheta, \varphi) \sin\vartheta \mathrm{d}\vartheta \mathrm{d}\varphi = 0 \tag{116}$$

According to Eq. 116, the spherical wave functions $\widetilde{\underline{F}}_{1nm}$ and $\widetilde{\underline{F}}_{2\overline{n}\overline{m}}$ are always orthogonal on the sphere even when $\overline{n} = n$ and $\overline{m} = m$. Moreover, it can be shown (Hald et al. 1988) that

$$\left\langle \widetilde{\underline{F}}_{1nm}, \widetilde{\underline{F}}_{1\overline{n}\overline{m}} \right\rangle = \left\langle \widetilde{\underline{F}}_{2nm}, \widetilde{\underline{F}}_{2\overline{n}\overline{m}} \right\rangle = 2\pi n(n+1) \delta_{m\overline{m}} \delta_{n\overline{n}} \tag{117}$$

where

$$\delta_{m\overline{m}} = \begin{cases} 1 & \text{for} \quad \overline{m} = m \\ 0 & \text{for} \quad \overline{m} \neq m \end{cases} \tag{118}$$

is the Kronecker delta.

In order to have orthonormal spherical wave functions and power-normalized spherical waves, it is convenient to introduce the new functions

$$\underline{F}_{1nm}(\vartheta, \varphi) = \left(\frac{-m}{|m|} \right)^m \frac{1}{\sqrt{2\pi n(n+1)}} \widetilde{\underline{F}}_{1nm}(\vartheta, \varphi) \tag{119}$$

$$\underline{F}_{2nm}(\vartheta, \varphi) = \left(\frac{-m}{|m|} \right)^m \frac{1}{\sqrt{2\pi n(n+1)}} \widetilde{\underline{F}}_{2nm}(\vartheta, \varphi) \tag{120}$$

The factor $(-m/|m|)^m$ ensures that the phase of the modes follows the phase of the spherical harmonics as defined by Edmonds (1974).

The transverse electric field radiated by the AUT on a sphere of radius r can be then rewritten in the form

$$\underline{E}_t = \beta \sum_{n=1}^{N_{\max}} \sum_{m=-n}^{n} \left[a_{1nm}\, g_{1n}(\beta r) \underline{F}_{1nm}(\vartheta, \varphi) + a_{2nm}\, g_{2n}(\beta r) \underline{F}_{2nm}(\vartheta, \varphi) \right] \tag{121}$$

The expression of the transverse electric field radiated by the AUT in its far-field region can be easily obtained from Eq. 121 by taking into account that

$$h_n^{(2)}(\beta r) \underset{\beta r \to \infty}{\approx} \mathrm{j}^{n+1} \frac{\mathrm{e}^{-\mathrm{j}\beta r}}{\beta r}; \quad \frac{1}{\beta r} \frac{\mathrm{d}}{\mathrm{d}(\beta r)} \left(\beta r h_n^{(2)}(\beta r) \right) \underset{\beta r \to \infty}{\approx} \mathrm{j}^n \frac{\mathrm{e}^{-\mathrm{j}\beta r}}{\beta r} \tag{122}$$

thus obtaining Eq. 52.

It is worth noting that, according to the Sommerfeld radiation conditions, in the far-field region the longitudinal electric field component E_r must vanish. Indeed, this is the case. As a matter of fact, each elementary TE^r spherical wave has no longitudinal component, whereas that relevant to a TM^r one decreases asymptotically as $1/r^2$ (Hald et al. 1988).

Nonredundant NF-FF Transformation Techniques

Nonredundant Sampling Representations of EM Fields

The main theoretical results concerning the nonredundant sampling representations of EM fields (Bucci et al. 1998c; Bucci and Gennarelli 2012) are summarized in this section. To this end, the field radiated by an arbitrary finite-size source enclosed in a convex domain $\mathcal{D}$, bounded by a surface Σ with rotational symmetry and observed on a regular surface $\mathcal{M}$ external to $\mathcal{D}$ and having the same symmetry, is considered. Due to its rotational symmetry, the surface $\mathcal{M}$ can be described by meridian curves and azimuthal circumferences, so that the field representation over a regular curve $\mathcal{C}$ described by a proper analytical parameterization $\underline{r} = \underline{r}(\xi)$ is considered in the following. Moreover, according to (Bucci et al. 1998c), it is convenient to define the reduced electric field

$$\underline{F}(\xi) = \underline{E}(\xi) \; e^{\mathrm{j}\gamma(\xi)} \tag{123}$$

where $\gamma(\xi)$ is a proper analytical phase function to be determined. As shown in (Bucci and Franceschetti 1987; Bucci et al. 1998c), the "band limitation" error, occurring when the reduced field $\underline{F}(\xi)$ is approximated by a spatially band-limited function, becomes negligible as the bandwidth exceeds the critical value

$$W_\xi = \max_\xi \left[w(\xi) \right] = \max_\xi \left[\max_{\underline{r}'} \left| \frac{\mathrm{d}\gamma(\xi)}{\mathrm{d}\xi} - \beta \frac{\partial R(\xi, \underline{r}')}{\partial \xi} \right| \right] \tag{124}$$

where $\underline{r}'$ denotes the source point and $R = \left| \underline{r}(\xi) - \underline{r}' \right|$. As a matter of fact, for large sources and observation domains not too near them, such an error exhibits a step-like behavior, decreasing more than exponentially as the bandwidth exceeds W_ξ (Bucci and Franceschetti 1987; Bucci et al. 1998c). As a consequence, it can be effectively controlled by choosing the bandwidth of the approximating function equal to $\chi' W_\xi$, where χ' is an enlargement bandwidth factor (slightly greater than unity for electrically large antennas).

In order to obtain a nonredundant representation, namely, a representation requiring a minimum number of samples, first of all, the "local" bandwidth $w(\xi)$ must be minimized for each ξ. This is accomplished by choosing γ such that its derivative is given by

$$\frac{\mathrm{d}\gamma}{\mathrm{d}\xi} = \frac{\beta}{2}\left[\max_{\underline{r}'}\frac{\partial R}{\partial s} + \min_{\underline{r}'}\frac{\partial R}{\partial s}\right]\frac{\mathrm{d}s}{\mathrm{d}\xi} = \frac{\beta}{2}\left[\max_{\underline{r}'}\mathbf{R}\cdot\mathbf{t} + \min_{\underline{r}'}\mathbf{R}\cdot\mathbf{t}\right]\frac{\mathrm{d}s}{\mathrm{d}\xi} \tag{125}$$

namely, $\mathrm{d}\gamma/\mathrm{d}\xi$ is the average between the maximum and minimum value of $\beta\partial R/\partial\xi$, when $\underline{r}'$ varies in the source domain $\mathcal{D}$. In Eq. 125, s is the curvilinear abscissa on $\mathcal{C}$, $\mathbf{t}$ is the unit vector tangent to $\mathcal{C}$ at the observation point P, and $\mathbf{R}$ is the unit vector pointing from the source point to P. Accordingly, the optimal phase factor to be used is given by

$$\gamma(\xi) = \frac{\beta}{2}\int_0^{s(\xi)}\left[\max_{\underline{r}'}\frac{\partial R}{\partial s} + \min_{\underline{r}'}\frac{\partial R}{\partial s}\right]\mathrm{d}s = \frac{\beta}{2}\int_0^{s}\left[\max_{\underline{r}'}\mathbf{R}\cdot\mathbf{t} + \min_{\underline{r}'}\mathbf{R}\cdot\mathbf{t}\right]\mathrm{d}s \tag{126}$$

It can be easily verified that, by choosing $\mathrm{d}\gamma/\mathrm{d}\xi$ according to Eq. 125, it results

$$w(\xi) = \frac{\beta}{2}\left[\max_{\underline{r}'}\frac{\partial R}{\partial s} - \min_{\underline{r}'}\frac{\partial R}{\partial s}\right]\frac{\mathrm{d}s}{\mathrm{d}\xi} = \frac{\beta}{2}\left[\max_{\underline{r}'}\mathbf{R}\cdot\mathbf{t} - \min_{\underline{r}'}\mathbf{R}\cdot\mathbf{t}\right]\frac{\mathrm{d}s}{\mathrm{d}\xi} \tag{127}$$

With reference to the parameter ξ, for avoiding redundancy, it must be determined by requiring that the local bandwidth is constant. In fact, if $w(\xi)$ is variable with ξ, the sample spacing, which is dictated by the bandwidth W_ξ, becomes unnecessarily small in the zones wherein $w(\xi)$ is smaller than its maximum value, giving rise to redundancy in the sampling representation. Accordingly, by imposing that $w(\xi)$ is constant and equal to W_ξ, it results

$$\xi = \frac{\beta}{2W_\xi}\int_0^{s}\left[\max_{\underline{r}'}\frac{\partial R}{\partial s} - \min_{\underline{r}'}\frac{\partial R}{\partial s}\right]\mathrm{d}s = \frac{\beta}{2W_\xi}\int_0^{s}\left[\max_{\underline{r}'}\mathbf{R}\cdot\mathbf{t} - \min_{\underline{r}'}\mathbf{R}\cdot\mathbf{t}\right]\mathrm{d}s \tag{128}$$

When $\mathcal{C}$ is a meridian curve (Fig. 17) and $\mathbf{t}$ is external to the cone of vertex P, tangent to Σ, the extreme values of $\mathbf{R}\cdot\mathbf{t}$ occur at the two tangency points $P_{1,2}$ on $\mathcal{C}'$ (intersection curve between the meridian plane and Σ). By taking into account that in such a case (Bucci et al. 1998c)

$$\left.\frac{\partial R}{\partial s}\right|_{s'_{1,2}} = \frac{\mathrm{d}R_{1,2}}{\mathrm{d}s} \pm \frac{\mathrm{d}s'_{1,2}}{\mathrm{d}s} \tag{129}$$

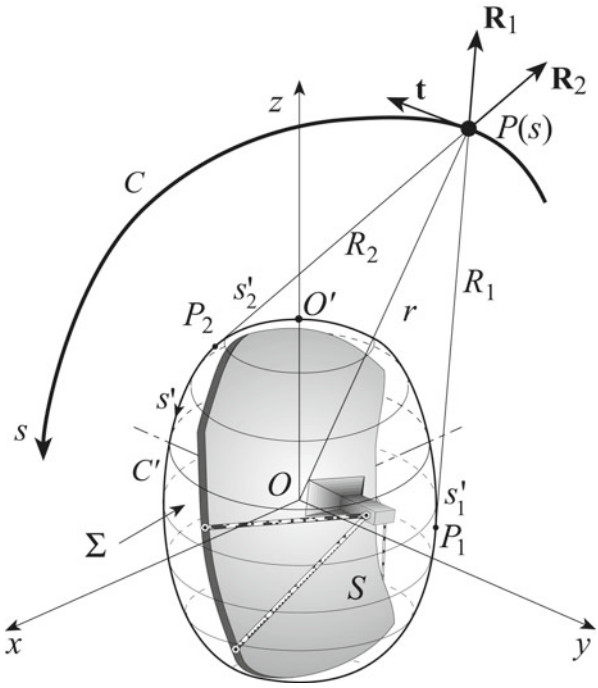

Fig. 17 Relevant to a meridian curve

where $s'_{1,2}$ are the arclength coordinates of $P_{1,2}$ and $R_{1,2}$ the distances from P to $P_{1,2}$ (Fig. 17) and choosing $W_\xi = \beta\ell'/2\pi$ (ℓ' being the length of $\mathcal{C}'$), it results

$$\gamma = \frac{\beta}{2}\left[R_1 + R_2 + s'_1 - s'_2\right] \tag{130}$$

$$\xi = \frac{\pi}{\ell'}\left[R_1 - R_2 + s'_1 + s'_2\right] \tag{131}$$

Note that the angular-like parameter ξ covers a 2π range when P encircles the source once and the number of samples at Nyquist spacing ($\Delta\xi = \pi/W_\xi$) on a closed meridian curve $\mathcal{C}$ (also unbounded) is always finite and equal to $N_\xi = 2\pi/\Delta\xi = 2\ell'/\lambda$.

It can be shown (Bucci et al. 1998c) that in any meridian plane the curves $\gamma =$ const and $\xi =$ const are orthogonal.

When $\mathcal{C}$ is an azimuthal circumference of radius ρ, the extreme values of $\mathbf{R}\cdot\mathbf{t}$ are opposite and constant along it. It follows from Eqs. 126 and 128 that γ is constant and any parameter proportional to the arclength is optimal. As a consequence, it is convenient to use the azimuthal angle φ as parameter and to choose for γ the value

relevant to any meridian curve passing through the observation point on $\mathcal{C}$. The corresponding bandwidth is (Bucci et al. 1998c)

$$W_\varphi = \frac{\beta}{2} \max_{z'} (R^+ - R^-)$$
$$= \frac{\beta}{2} \max_{z'} \left(\sqrt{(z - z')^2 + (\rho + \rho'(z'))^2} - \sqrt{(z - z')^2 + (\rho - \rho'(z'))^2} \right) \quad (132)$$

where R^+ and R^- are the maximum and minimum distance, respectively, from each circumference describing the surface Σ to the observation point P and $\rho'(z')$ is the equation of Σ in cylindrical coordinates. As shown in (Bucci et al. 1998c), the maximum is attained on that zone of the surface Σ lying on the same side of the observation circumference with respect to the maximum transverse circle of Σ. When the radius of the observation circle goes to infinity, it results $R^+ = R^- + 2\rho' \sin\vartheta$ and, accordingly,

$$W_\varphi = \beta \rho'_{\max} \sin\vartheta \quad (133)$$

ϑ being the polar angle of the circle points and $\rho'_{\max}$ the maximum transverse radius of Σ.

It can be shown (Bucci et al. 1998c) that the number of samples N_s at Nyquist spacing on any closed observation surface (also unbounded) surrounding the source is

$$N_s \cong (\text{area of } \Sigma)/(\lambda/2)^2 \quad (134)$$

Any finite-size source can be always considered as enclosed in a spherical surface. Accordingly, by choosing Σ coincident with a sphere of radius a, for any meridian curve, it results

$$R_1 = R_2 = \sqrt{r^2 - a^2} \quad (135)$$

$$s'_1 = (\vartheta - \alpha)a; \quad s'_2 = (\vartheta + \alpha)a; \quad \alpha = \cos^{-1}(a/r) \quad (136)$$

Accordingly, since $\ell' = 2\pi a$, it results $W_\xi = \beta a$ and

$$\gamma = \beta\sqrt{r^2 - a^2} - \beta a \cos^{-1}(a/r); \quad \xi = \vartheta \quad (137)$$

When considering an azimuthal circumference, by putting $z' = a \cos\vartheta'$ and $\rho' = a \sin\vartheta'$, it can be shown (Bucci et al. 1998c) that the maximum in Eq. 132 is attained at $\vartheta' = \cos^{-1}(a \cos\vartheta/r)$ and, accordingly,

$$W_\varphi = \beta a \sin\vartheta \quad (138)$$

Eq. 134 highlights the role that the source modeling plays in minimizing the overall number of samples: the surface Σ must fit very well the antenna geometry, moreover it must be analytically regular and such that the corresponding phase factor and parameterization are simple to be determined. To this end, ellipsoidal geometries (oblate and prolate) are considered in the following.

An effective modeling for elongated antennas is obtained by choosing the surface Σ coincident with a rotational prolate ellipsoid, having major and minor semiaxes equal to a and b (Fig. 18), whereas a rotational oblate ellipsoid is an appropriate modeling for quasiplanar sources. In both the cases, it can be shown (Bucci et al. 1998c) that in any meridian plane the curves $\gamma = \text{const}$ and $\xi = \text{const}$ are respectively ellipses and hyperbolas confocal to $\mathcal{C}'$. This implies that ξ and γ are functions of the elliptic coordinates $u = (r_1 - r_2)/2f$ and $v = (r_1 + r_2)/2a$, respectively, where $r_{1,2}$ are the distances from the observation point P on the meridian plane to the foci of $\mathcal{C}'$ and $2f$ is the focal distance. By taking into account that the length of the ellipse $\mathcal{C}'$ is $\ell' = 4aE(\pi/2|\varepsilon^2)$, the bandwidth W_ξ becomes

$$W_\xi = (4a/\lambda)E(\pi/2|\varepsilon^2) \tag{139}$$

where $E(\cdot|\cdot)$ denotes the elliptic integral of second kind and $\varepsilon = f/a$ is the eccentricity of $\mathcal{C}'$.

The evaluation of γ at P can be simplified by considering the intersection point between the confocal ellipse through P and the symmetry axis, instead of P itself, since the same value of γ corresponds to all points lying on a confocal ellipse. By straightforward but lengthy computations, from Eq. 130, it results (Bucci et al. 1998c)

$$\gamma = \beta a \left[v\sqrt{\frac{v^2-1}{v^2-\varepsilon^2}} - E\left(\cos^{-1}\sqrt{\frac{1-\varepsilon^2}{v^2-\varepsilon^2}}|\varepsilon^2 \right) \right] \tag{140}$$

With reference to ξ, since the same value corresponds to all points on the confocal hyperbola branch passing through P, it can be convenient to consider, instead of P itself, the intersection point P_0 between the considered hyperbola branch and $\mathcal{C}'$. Accordingly from Eq. 131, it results $\xi = 2\pi s_0'/\ell'$, s_0' being the curvilinear abscissa of P_0. By straightforward computations, the following expression is finally obtained (Bucci et al. 1998c):

$$\xi = \frac{\pi}{2}\begin{cases} E(\sin^{-1}u|\varepsilon^2)/E(\pi/2|\varepsilon^2) + 1 & \text{prolate ellipsoid} \\ E(\sin^{-1}u|\varepsilon^2)/E(\pi/2|\varepsilon^2) & \text{oblate ellipsoid} \end{cases} \tag{141}$$

Such a relation is valid when the angle ϑ corresponding to P belongs to the range $[0, \pi/2]$. The case in which ϑ belongs to $[\pi/2, \pi]$ can be easily handled by determining the value ξ' corresponding to the point specified by the angle $\pi - \vartheta$ and then putting $\xi = \pi - \xi'$.

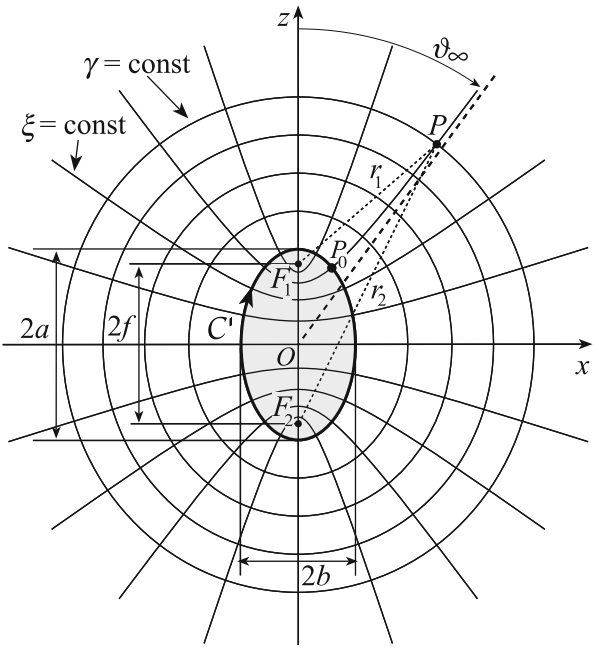

Fig. 18 Ellipsoidal source modeling: prolate case

Since all transverse circles belonging to the hyperboloid of rotation fixed by a value of ξ are characterized by the same value of W_φ (Bucci et al. 1998c), the bandwidth value corresponding to an azimuthal circumference can be evaluated by moving such a circle to infinity along the hyperbola $\xi = \text{const}$. Accordingly, by taking Eq. 133 into account, it results

$$W_\varphi(\xi) = \begin{cases} \beta b \sin \vartheta_\infty(\xi) & \text{prolate ellipsoid} \\ \beta a \sin \vartheta_\infty(\xi) & \text{oblate ellipsoid} \end{cases} \tag{142}$$

where

$$\vartheta_\infty = \begin{cases} \sin^{-1} u + \pi/2 & \text{prolate ellipsoid} \\ \sin^{-1} u & \text{oblate ellipsoid} \end{cases} \tag{143}$$

is the polar angle of the asymptote to the hyperbola through P (see Fig. 18).

It can be easily shown (Bucci et al. 1998c) that the spherical modeling can be obtained from the prolate or oblate ellipsoidal one by considering an ellipsoid with eccentricity $\varepsilon = 0$.

Another effective source modeling for long antennas is obtained by choosing the surface Σ coincident with a rounded cylinder (Fig. 19), namely, a cylinder of height h' ended in two half-spheres of radius a' (Bucci et al. 1998b; D'Agostino et al. 2011). Such a modeling is quite general and contains the spherical one as particular case. When considering quasiplanar antennas, a convenient alternative to the oblate ellipsoidal modeling is the two-bowls one (Fig. 20), wherein Σ is a surface formed

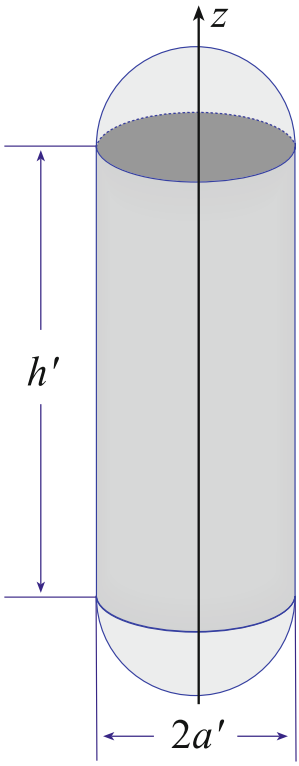

Fig. 19 Rounded cylinder modeling

by two circular bowls with the same aperture diameter, but with bending radii c and c' of the upper and lower arcs eventually different to fit better the actual AUT geometry (Bucci et al. 1998a; D'Agostino et al. 2011). It can be easily recognized that the surface Σ coincides with a sphere if $c = c' = a$, it becomes a half-sphere if $c = 0$ and $c' = a$, and it reduces to a circular dish for $c = c' = 0$.

The real part of the electric field and reduced electric field y-component radiated by an antenna along a line is reported in Fig. 21 to show the effect of multiplying the field by the factor $e^{j\gamma(\xi)}$. The considered antenna is a uniform planar circular array with radius equal to 20λ, lying in the plane $z = 0$, and has been modeled by an oblate ellipsoid with $2a = 40\lambda$ and $2b = 5\lambda$. The array elements, radially and azimuthally spaced of 0.8λ, are elementary Huygens sources linearly polarized along the y axis. The considered straight line is the x-directed line at $y = 0$, lying in a plane at distance $d = 12\lambda$ from the AUT center. As can be seen, the spatial variations of the reduced field component are slower than the electric field ones, since the local bandwidth has been minimized. Quite analogous results are obtained for the imaginary part.

In order to highlight the role of the optimal parameter for a convenient representation of the reduced field on the observation curve, the real part of the reduced electric field y-component along the same straight line is plotted as function of ξ in Fig. 22.

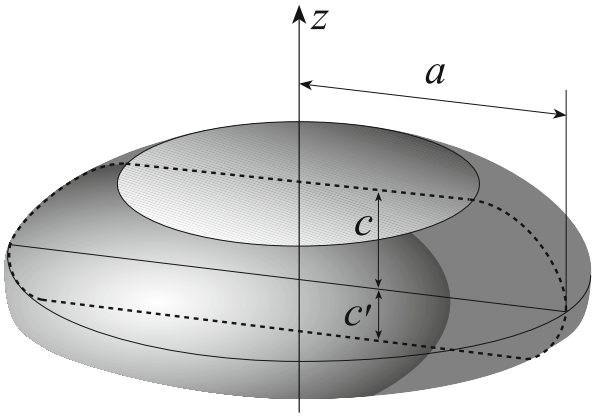

Fig. 20 Two-bowls modeling

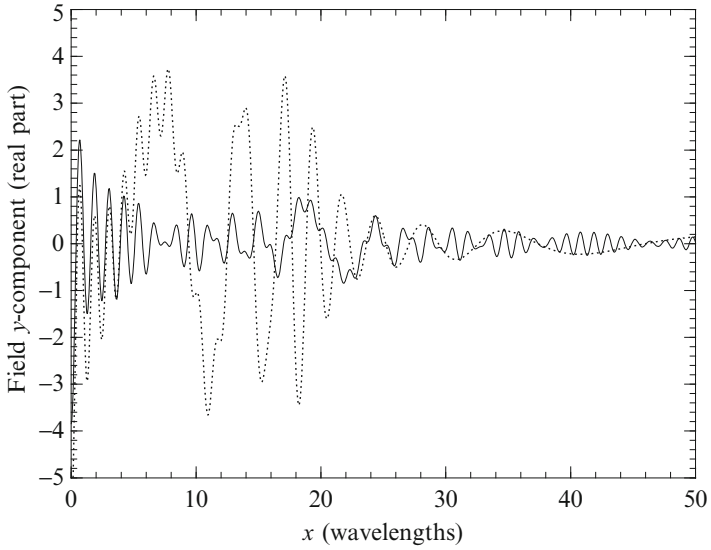

Fig. 21 Real part of the NF *y*-component on the given line. *Solid line*: electric field. *Dashed line*: reduced field

As can be seen, when using the optimal parameter, the regions wherein the reduced field exhibits fast changes are represented in an enlarged scale, whereas those characterized by slow variations are shown in a reduced scale. As a consequence, a uniform sampling in ξ gives rise to a denser sample distribution where the local bandwidth w is greater and to a sparser one in the zones characterized by smaller values of w (see Fig. 23).

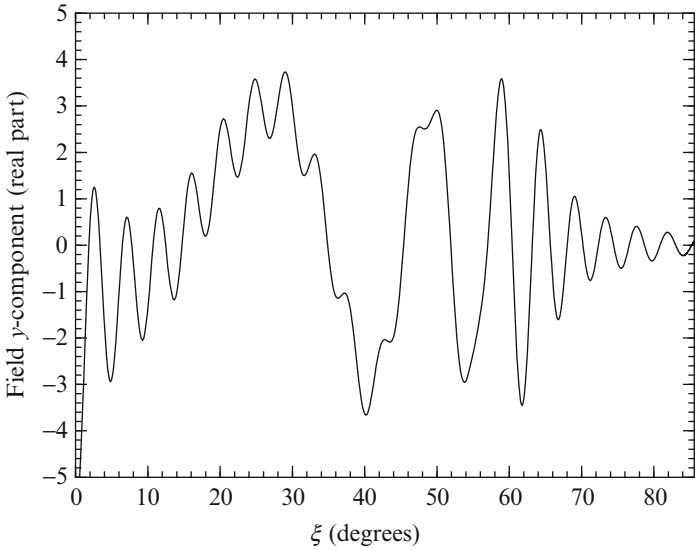

Fig. 22 Real part of the reduced electric field y-component on the given line as function of the optimal parameter ξ

Application of the Nonredundant Sampling Representations to the NF-FF Transformations

Let an antenna be considered as enclosed in a convex domain bounded by a rotational surface Σ, and the surface scanned by a nondirective probe be obtained by rotating a meridian curve always external to the cone of vertex at the observation point P and tangent to Σ. Since the voltage V measured by such a kind of probe has practically the same effective spatial bandwidth of the AUT field (Bucci et al. 1998d), the above described nonredundant sampling representations of EM fields can be applied to it and, accordingly, it is convenient to introduce the reduced voltage $\tilde{V}(\xi) = V(\xi)e^{j\gamma(\xi)}$.

Therefore, the use of cardinal series (CS) expansions (Whittaker 1915) springs out naturally as an appropriate tool to conveniently represent it. However, the use of the CS representation, while completely satisfactory from the accuracy point of view, has the drawback that all samples (or, at least, all the relevant ones) must be considered in evaluating the voltage at each output point, otherwise a relatively large truncation error is introduced, due to the slow decay of the sampling functions. As a consequence, its use would lead to unacceptably large computational times. Such a slow decay leads to a further, subtler difficulty, if it is taken into account that, in any practical instance, the measured data are inaccurate. Provided that their values are well above the noise level, the measured results are usually affected by an

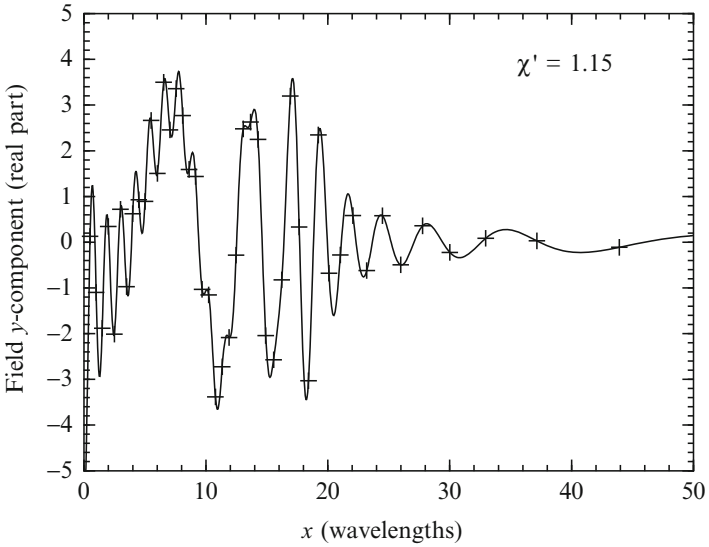

Fig. 23 Samples distribution on the given line

(approximately) constant relative, not absolute, error, so that the absolute error corresponding to the highest voltage values can be relatively large. This error is spread out by the sampling functions without a severe attenuation, and this gives rise to a remarkable relative error in the zones where the voltage level is low (Bucci et al. 1991b). These difficulties have been overcome by resorting to an OSI expansion (Bucci et al. 1991a, b), in which only relatively few samples in the neighborhood of the output point are used in the reconstruction. These algorithms minimize the truncation error for a given number of retained samples and are more stable than the CS expansions with respect to random errors affecting the data.

In the light of the above discussion, the voltage at $P\,(\xi(\vartheta), \varphi)$ on the meridian curve fixed by φ can be efficiently evaluated via the OSI expansion (Bucci et al. 1998c; Bucci and Gennarelli 2012):

$$V(\xi(\vartheta),\varphi) = \mathrm{e}^{-\mathrm{j}\gamma(\xi)}\tilde{V}(\xi,\varphi) = \mathrm{e}^{-\mathrm{j}\gamma(\xi)} \sum_{m=m_0-q+1}^{m_0+q} \tilde{V}(\xi_m,\varphi)\Omega_M\left(\xi-\xi_m,\overline{\xi}\right)D_{M''}(\xi-\xi_m) \tag{144}$$

where $m_0 = \mathrm{Int}(\xi/\Delta\xi)$ is the index of sample nearest (on the left) to P, $2q$ is the number of the retained intermediate samples $\tilde{V}(\xi_m, \varphi)$, namely, the reduced voltages at the intersection points between the sampling azimuthal circumferences and the meridian curve, $\overline{\xi} = q\Delta\xi$, $M = M'' - M'$, and

$$\xi_m = m\Delta\xi = 2\pi m/(2M''+1); \quad M'' = \mathrm{Int}(\chi M') + 1; \quad M' = \mathrm{Int}(\chi' W_\xi) + 1 \tag{145}$$

χ being an oversampling factor required to control the truncation error (Bucci et al. 1991a, 1998c), and Int(x) denoting the integer part of x. Moreover,

$$D_{M''}(\xi) = \frac{\sin\left[(2M''+1)\xi/2\right]}{(2M''+1)\sin(\xi/2)}; \quad \Omega_M\left(\xi,\overline{\xi}\right) = \frac{T_M\left[2\cos^2(\xi/2)/\cos^2\left(\overline{\xi}/2\right)-1\right]}{T_M\left[2/\cos^2\left(\overline{\xi}/2\right)-1\right]} \tag{146}$$

are the Dirichlet and Tschebyscheff sampling functions, respectively, $T_M(\cdot)$ being the Tschebyscheff polynomial of degree M.

It is worth noting that the weight function $\Omega_M(\cdot,\cdot)$ has been obtained in (Bucci et al. 1991a, b) by paralleling the properties of the so-called sampling window function introduced by Knab (1983), which (in the square norm) represents the practically optimal weight function for the case of an indefinite observation domain, where the kernel of the CS expansion is the $\sin(x)/x$ function instead of the Dirichlet one.

The intermediate samples $\tilde{V}(\xi_m, \varphi)$ can be determined by means of the OSI formula:

$$\tilde{V}(\xi_m,\varphi) = \sum_{n=n_0-p+1}^{n_0+p} \tilde{V}\left(\xi_m,\varphi_{n,m}\right)\Omega_{N_m}\left(\varphi-\varphi_{n,m},\overline{\varphi}\right)D_{N_m''}\left(\varphi-\varphi_{n,m}\right) \tag{147}$$

where $n_0 = \mathrm{Int}(\varphi/\Delta\varphi_m)$, $\tilde{V}(\xi_m, \varphi_{n,m})$ are the reduced samples on the azimuthal circumference fixed by ξ_m, $2p$ is the retained samples number, and

$$\varphi_{n,m} = n\Delta\varphi_m = 2\pi n/\left(2N_m''+1\right); \quad N_m'' = \mathrm{Int}\left(\chi N_m'\right)+1; \quad N_m' = \mathrm{Int}\left[\chi * W_\varphi(\xi_m)\right]+1 \tag{148}$$

$$\overline{\varphi} = p\Delta\varphi_m; \quad N_m = N_m'' - N_m'; \quad \chi^* = 1+(\chi'-1)\left[\sin\vartheta(\xi_m)\right]^{-2/3} \tag{149}$$

The variation of the azimuthal enlargement bandwidth factor χ^* with ξ is required to ensure a band limitation error constant with respect to ξ (Bucci and Franceschetti 1987).

By properly matching Eqs. 144 and 147, the two-dimensional OSI expansion is obtained:

$$V(\xi(\vartheta),\varphi) = \mathrm{e}^{-\mathrm{j}\gamma(\xi)} \sum_{m=m_0-q+1}^{m_0+q} \left\{ \Omega_M\left(\xi-\xi_m,\overline{\xi}\right)D_{M''}(\xi-\xi_m) \cdot \sum_{n=n_0-p+1}^{n_0+p} \tilde{V}\left(\xi_m,\varphi_{n,m}\right)\Omega_{N_m}\left(\varphi-\varphi_{n,m},\overline{\varphi}\right)D_{N_m''}\left(\varphi-\varphi_{n,m}\right) \right\} \tag{150}$$

which makes possible to reconstruct efficiently and accurately the NF data needed to carry out the traditional NF-FF transformation corresponding to the considered

scanning geometry from a nonredundant, i.e., minimum, number of NF measurements.

Efficient and accurate NF-FF transformation techniques with plane-polar (Bucci et al. 1998a, 2000), bipolar (D'Agostino et al. 2003), cylindrical (Bucci et al. 1998b; D'Agostino et al. 2002), and spherical (Bucci et al. 2001a; D'Agostino et al. 2011, 2013a) scannings have been so developed. In all the cases, a remarkable reduction of the number of the required NF data and of the related measurement time has been achieved.

The effectiveness of the OSI algorithms depends on the choice of the following parameters: the enlargement bandwidth factor, the oversampling factor, and the retained samples number. The enlargement bandwidth factor χ' allows to control the aliasing error and values slightly greater than unity are enough to ensure small errors in the case of electrically large antennas (Bucci and Franceschetti 1987, 1989). A numerical procedure to properly select the χ' value is described in (Gennarelli et al. 1994). As regards the choice of the parameters controlling the truncation error, namely, the oversampling factor χ, and the numbers p, q of the retained nearest samples, it can be numerically made as in (Bucci et al. 1998c). Note that such an error can be decreased on increasing p, q, and/or χ. An increase of p, q implies a growth of the interpolation time, whereas an increase of χ reflects in a growth of the required NF data and, as a consequence, of the measurement time. In practice, the choice of the above parameters is done in such a way that the error related to the interpolation (aliasing plus truncation) must be smaller than the measurement one (background noise plus measurement uncertainties). It must stressed that, due to the filtering properties of the interpolation functions, it is possible also to cut away the spatial harmonics relevant to the noise sources outside the AUT spatial bandwidth.

NF-FF Transformation Techniques with Spiral Scannings

The scanning of a nondirective probe along a proper spiral wrapping an arbitrary rotational surface $\mathcal{M}$, obtained by rotating a meridian curve always external to the cone having the vertex at P and tangent to the rotational surface Σ enclosing the AUT, is considered in the following. The Cartesian coordinates of a generic point on such a spiral are

$$\begin{cases} x = r(\theta)\sin\theta\cos\phi \\ y = r(\theta)\sin\theta\sin\phi \\ z = r(\theta)\cos\theta \end{cases} \tag{151}$$

where $r(\theta)$ is specified by the meridian curve generating the surface $\mathcal{M}$, ϕ is the angular parameter describing the spiral, and the angle θ is a monotonic increasing function of ϕ. It can be easily verified that $r(\theta) = d/\cos\theta$ in the case of a planar spiral lying on a plane at distance d, $r(\theta) = d/\sin\theta$ for a helix wrapping a cylinder of radius d, whereas $r(\theta) = d$ when a spherical spiral is considered. It is worth noting that the

angle θ, unlike the zenithal angle ϑ, can assume negative values. As a matter of fact, when the spiral describes a complete round on the surface $\mathcal{M}$, moving from the south pole to the north pole and then returning to the south one, θ varies in the range $[-\pi, \pi]$. Moreover, ϕ is always continuous, whereas, according to Eq. 151, the azimuthal angle φ displays a discontinuity jump of π when the spiral crosses the poles.

In order to obtain a nonredundant sampling representation of the probe voltage on the surface $\mathcal{M}$ from its samples collected along the spiral, it is necessary (D'Agostino et al. 2009e; Cicchetti et al. 2014):

(a) to choose the spiral in such a way that its pitch, specified by two consecutive intersections (at ϕ and $\phi + 2\pi$) with a meridian curve, be equal to the sample spacing needed for the interpolation along this curve;
(b) to develop a nonredundant sampling representation along the spiral.

According to condition (a), the optimal parameter ξ relevant to the meridian curve and the angular one ϕ describing the spiral are related by

$$\xi = k\phi \tag{152}$$

where k must be such that the interval $\Delta\xi = 2\pi k$, corresponding to the spiral pitch, is equal to the required sample spacing $\Delta\xi = 2\pi/(2\,M'' + 1)$ (see Eq. 145). Accordingly, $k = 1/(2\,M'' + 1)$. The scanning spiral can be so viewed as the projection on the surface $\mathcal{M}$, via the curves at $\xi = \text{const}$, of the corresponding spiral wrapping with the same pitch the modeling surface Σ.

The development of a nonredundant sampling representation of the voltage along the spiral is a more complex task, which has been heuristically solved in (D'Agostino et al. 2009e) by paralleling the rigorous procedure (D'Agostino et al. 2006) valid when the antenna is modeled by a spherical surface. Therefore, the main results of the unified theory of spiral scannings for antennas enclosed in a spherical surface (D'Agostino et al. 2006) are reviewed in the following.

In such a case, the optimal parameter to describe a meridian curve is the angle θ (which coincides in the range $[0, \pi]$ with the zenithal one ϑ) and the related bandwidth is βa. Moreover, the optimal phase factor ψ and parameter η to obtain a nonredundant representation along the spiral can be obtained from Eqs. 126 and 128 by observing that the extreme values of $\mathbf{R} \cdot \mathbf{t}$ occur (D'Agostino et al. 2006) at the two tangency points $P_{1,2}$ (Fig. 24) between the sphere modeling the AUT and the straight lines passing through the point Q on the spiral and belonging to the plane specified by the unit vectors $\mathbf{t}$ (tangent to the spiral at Q) and $\mathbf{r}$ (pointing from the origin to Q). Denoting by $\mathbf{R}_{1,2}$ the related unit vectors and by δ the angle between $\mathbf{r}$ and $\mathbf{t}$ (see Fig. 24), it results (D'Agostino et al. 2006)

$$(\mathbf{R}_1 + \mathbf{R}_2)/2 = \mathbf{r}\sin\alpha = \mathbf{r}\sqrt{1 - a^2/r^2} \tag{153}$$

$$(\mathbf{R}_1 - \mathbf{R}_2)/2 = \mathbf{n}\cos\alpha \tag{154}$$

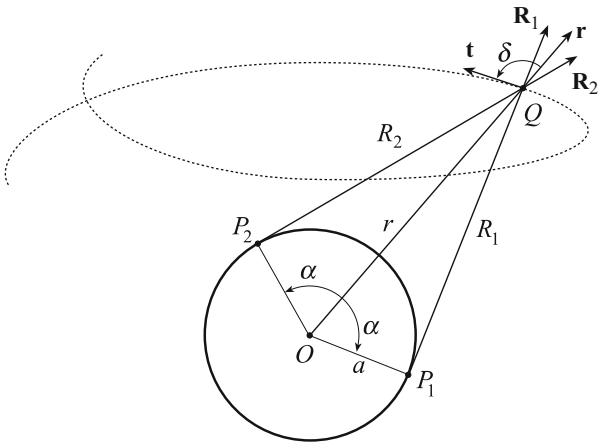

Fig. 24 Geometry of the problem in the plane **t**, **r**

where **n** is the unit vector parallel to the plane **r**, **t** and orthogonal to **r**. Accordingly

$$(\mathbf{R}_1 - \mathbf{R}_2) \cdot \mathbf{t}/2 = (\mathbf{n} \cdot \mathbf{t})\,(a/r) = (a/r)\sin\delta \tag{155}$$

By substituting Eq. 153 in Eq. 126 and taking into account that $\mathrm{d}r = \mathbf{r} \cdot \mathbf{t}\,\mathrm{d}s$, it results

$$\psi = \beta \int_0^r \sqrt{1 - a^2/r^2}\,\mathrm{d}r = \beta\sqrt{r^2 - a^2} - \beta a \cos^{-1}(a/r) \tag{156}$$

Namely, the phase function ψ relevant to the sampling representation along the spiral coincides with that γ related to the representation on a meridian curve.

By differentiating Eq. 151, it can be easily verified that

$$\mathrm{d}s = \sqrt{r^2 \sin^2\theta + k^2 r^2 + k^2 \dot{r}^2}\,\mathrm{d}\phi \tag{157}$$

where $\dot{r} = \mathrm{d}r/\mathrm{d}\theta$. Moreover,

$$\mathbf{r} \cdot \mathbf{t} = \frac{\mathrm{d}r}{\mathrm{d}s} = \frac{\mathrm{d}r}{\mathrm{d}\phi}\frac{\mathrm{d}\phi}{\mathrm{d}s} = \left[\frac{\mathrm{d}r}{\mathrm{d}\theta}\frac{\mathrm{d}\theta}{\mathrm{d}\phi}\right]\frac{\mathrm{d}\phi}{\mathrm{d}s} = k\dot{r}\frac{\mathrm{d}\phi}{\mathrm{d}s} = \frac{k\dot{r}}{\sqrt{r^2 \sin^2\theta + k^2 r^2 + k^2 \dot{r}^2}} \tag{158}$$

and, accordingly,

$$\sin\delta = \sqrt{1 - (\mathbf{r} \cdot \mathbf{t})^2} = \sqrt{\frac{r^2 \sin^2\theta + k^2 r^2}{r^2 \sin^2\theta + k^2 r^2 + k^2 \dot{r}^2}} \tag{159}$$

By substituting Eqs. 155 and 157 in Eq. 128 and taking into account Eq. 159, it results

$$\eta = \frac{\beta a}{W_\eta} \int_0^\phi \sqrt{k^2 + \sin^2 k\phi}\ \mathrm{d}\phi \tag{160}$$

that is, the optimal parameter η for describing the spiral is β/W_η times the arclength of the projecting point that lies on the spiral wrapping the sphere Σ. Since such a spiral is a closed curve, it is convenient to choose the bandwidth W_η in such a way that the angular-like parameter η covers a 2π range when the entire projecting spiral is described. Therefore,

$$W_\eta = \frac{\beta a}{\pi} \int_0^{(2M''+1)\pi} \sqrt{k^2 + \sin^2 k\phi}\ \mathrm{d}\phi \tag{161}$$

namely, the bandwidth W_η is β/π times the length of the spiral which wraps from pole to pole the sphere Σ.

The more general case wherein the AUT is no longer modeled as enclosed in a sphere is now considered. The parameterization η for describing the scanning spiral, the related phase factor ψ, and bandwidth W_η can be heuristically obtained (D'Agostino et al. 2009e) by generalizing the corresponding ones for the spherical modeling case (see Eqs. 160, 156, and 161). In particular, η is β/W_η times the arclength of the projecting point that lies on the spiral wrapping the surface Σ (the projection is obtained by the curves at $\xi = \text{const}$ that, in such a case, take the role of the radial lines of the spherical modeling), ψ coincides with the phase function γ for a meridian curve, and the bandwidth W_η is β/π times the length of the spiral wrapping Σ from pole to pole. In other words, the spiral, ψ, and η coincide with those relevant to the spherical modeling when the surface Σ approaches a sphere.

In the light of the above results, the reduced voltage at any point Q of the spiral can be reconstructed by the following OSI expansion (D'Agostino et al. 2006, 2009e; Cicchetti et al. 2014):

$$\tilde{V}(\eta) = \sum_{n=n_0-p+1}^{n_0+p} \tilde{V}(\eta_n)\Omega_N(\eta - \eta_n, \overline{\eta}) D_{N''}(\eta - \eta_n) \tag{162}$$

where $2p$ is the number of retained samples $\tilde{V}(\eta_n)$, $n_0 = \mathrm{Int}(\eta/\Delta\eta)$ is the index of the sample nearest (on the left) to the point Q, $\overline{\eta} = p\Delta\eta$, $N = N'' - N'$, and

$$\eta_n = n\Delta\eta = 2\pi n/(2N'' + 1); \quad N'' = \mathrm{Int}(\chi N') + 1; \quad N' = \mathrm{Int}\left(\chi' W_\eta\right) + 1 \tag{163}$$

It must be stressed that small variations of η correspond to very large changes of ϕ in the neighborhood of the poles ($\vartheta = 0$ and $\vartheta = \pi$), so that, when interpolating the voltage in these zones, the enlargement bandwidth factor χ' must be properly increased to avoid a significant growth of the band limitation error.

The expansion (Eq. 162) can be used to determine the "intermediate samples," namely, the reduced voltage values at the intersection points between the meridian curve passing through the observation point P and the spiral. Once they have been determined, the voltage at the point P can be recovered by means of the following OSI expansion:

$$V(\xi(\vartheta),\varphi) = \mathrm{e}^{-\mathrm{j}\gamma(\xi)} \sum_{m=m_0-q+1}^{m_0+q} \tilde{V}(\xi_m)\Omega_M\left(\xi-\xi_m,\overline{\xi}\right)D_{M''}(\xi-\xi_m) \tag{164}$$

where $2q$ is the number of retained intermediate samples $\tilde{V}(\xi_m)$, $m_0 = \mathrm{Int}\,[(\xi - \xi_0)/\Delta\xi]$ is the index of the sample nearest (on the left) to the point P, $M = M'' - M'$, $\overline{\xi} = q\Delta\xi$, and

$$\xi_m = \xi_m(\varphi) = k\varphi + m\Delta\xi = \xi_0 + m\Delta\xi \tag{165}$$

Summary

The aim of this chapter is to provide a complete description of the NF antenna measurement techniques to students, junior engineers, researchers, and physicists that wish to tackle such a topic. To this end, a wide introduction resumes the state of the art by supplying also a rich and updated bibliography. Then, the classical NF-FF transformations with plane-rectangular, cylindrical, and spherical scannings, in their probe-uncompensated and probe-compensated versions, are summarized by pointing out their advantages and drawbacks. Moreover, some analytical details on the wave expansions commonly employed to represent the antenna field in the region external to it are reported in order to enable the interested reader to achieve a more in-depth knowledge of the topic. The nonredundant sampling representations of the electromagnetic fields are then introduced, highlighting how their application to the NF-FF transformations with conventional scannings allows a drastic measurement time reduction with respect to the classical ones, without any loss in accuracy of the FF reconstruction. At last, the NF-FF transformations using innovative spiral scannings, which allow a further measurement time saving by exploiting continuous and synchronized movements of the positioning systems, are described. They employ efficient sampling representations to accurately reconstruct the probe voltage on a quite arbitrary rotational surface from a nonredundant number of its samples collected on a proper spiral wrapping it.

Cross-References

► Anechoic Chamber Design
► Antenna Measurement Setups: Introduction
► EMI/EMC Chamber Design, Measurement, and Instrument

► Mm-wave Sub-mm-wave Antenna Measurement
► Radiation Efficiency Measurements of Small Antennas

References

Alvarez Y, Las-Heras F, Pino M (2008) Probe-distortion correction for the sources reconstruction method. Antennas Propag Mag IEEE 50(6):117–124
Appel-Hansen J (1980) On cylindrical near-field scanning techniques. Antennas Propag IEEE Trans 28(2):231–234
Appel-Hansen J, Dyson J, Gillespie E, Hickman T (1982) Antenna measurements, chap. 8. In: Rudge A, Milne K, Olver A, Knight P (eds) The handbook of antenna design, Electromagnetic waves. Peter Peregrinus, London, pp 584–694
Balanis C (1989) Advanced engineering electromagnetics. Wiley, New York
Balanis C (1997) Antenna theory – analysis and design, 2nd edn. Wiley, New York
Belousov S (1962) Tables of normalized associated legendre polynomials. Pergamon Press, Oxford
Bennett J, Anderson A, McInnes P, Whitaker A (1976) Microwave holographic metrology of large reflector antennas. Antennas Propag IEEE Trans 24(3):295–303
Bolomey J, Cown B, Fine G, Jofre L, Mostafavi M, Picard D, Estrada J, Friederich P, Cain F (1988) Rapid near-field antenna testing via arrays of modulated scattering probes. Antennas Propag IEEE Trans 36(6):804–814
Brigham E (1974) The fast fourier transform. Prentice Hall, Englewood Cliffs
Bruning J, Lo Y (1971) Multiple scattering of EM waves by spheres part I – multipole expansion and ray-optical solutions. Antennas Propag IEEE Trans 19(3):378–390
Bucci O, Franceschetti G (1987) On the spatial bandwidth of scattered fields. Antennas Propag IEEE Trans 35(12):1445–1455
Bucci O, Franceschetti G (1989) On the degrees of freedom of scattered fields. Antennas Propag IEEE Trans 37(7):918–926
Bucci O, Gennarelli C (2012) Application of nonredundant sampling representations of electromagnetic fields to NF-FF transformation techniques. Int J Antennas Propag 2012, 319856, 14 pages
Bucci O, D'Elia G, Leone G, Pierri R (1990) Far-field pattern determination from the near-field amplitude on two surfaces. Antennas Propag IEEE Trans 38(11):1772–1779
Bucci O, Gennarelli C, Savarese C (1991a) Fast and accurate near-field – far-field transformation by sampling interpolation of plane-polar measurements. Antennas Propag IEEE Trans 39(1):48–55
Bucci O, Gennarelli C, Savarese C (1991b) Optimal interpolation of radiated fields over a sphere. Antennas Propag IEEE Trans 39(11):1633–1643
Bucci O, Gennarelli C, Riccio G, Savarese C (1998a) Near-field – far-field transformation from nonredundant plane-polar data: effective modellings of the source. Microwaves Antennas Propag IEE Proc 145(1):33–38
Bucci O, Gennarelli C, Riccio G, Savarese C (1998b) NF-FF transformation with cylindrical scanning: an effective technique for elongated antennas. Microwaves Antennas Propag IEE Proc 145(5):369–374
Bucci O, Gennarelli C, Savarese C (1998c) Representation of electromagnetic fields over arbitrary surfaces by a finite and nonredundant number of samples. Antennas Propag IEEE Trans 46 (3):351–359
Bucci O, D'Elia G, Migliore M (1998d) Advanced field interpolation from plane-polar samples: experimental verification. Antennas Propag IEEE Trans 46(2):204–210
Bucci O, D'Elia G, Migliore M (1999) An effective near-field far-field transformation technique from truncated and inaccurate amplitude-only data. Antennas Propag IEEE Trans 47 (9):1377–1385

Bucci O, D'Agostino F, Gennarelli C, Riccio G, Savarese C (2000) NF-FF transformation with plane-polar scanning: ellipsoidal modelling of the antenna. Automatika 41(3–4):159–164
Bucci O, D'Agostino F, Gennarelli C, Riccio G, Savarese C (2001a) Data reduction in the NF-FF transformation technique with spherical scanning. J Electromagn Waves Appl 15(6):755–775
Bucci O, Gennarelli C, Riccio G, Savarese C (2001b) Nonredundant NF-FF transformation with helicoidal scanning. J Electromagn Waves Appl 15(11):1507–1519
Bucci O, D'Agostino F, Gennarelli C, Riccio G, Savarese C (2002) Probe compensated far-field reconstruction by near-field planar spiral scanning. Microwaves Antennas Propag IEE Proc 149 (2):119–123
Bucci O, D'Agostino F, Gennarelli C, Riccio G, Savarese C (2003) Near-field – far-field transformation with spherical spiral scanning. Antennas Wirel Propag Lett IEEE 2(1):263–266
Cicchetti R, D'Agostino F, Ferrara F, Gennarelli C, Guerriero R, Migliozzi M (2014) Near-field to far-field transformation techniques with spiral scannings: a comprehensive review. Int J Antennas Propag 2014, 143084, 13 pages
Clemmow P (1966) The plane wave spectrum representation of electromagnetic fields. Pergamon, London
Corona P, Ferrara G, Gennarelli C (1989) Measurement distance requirements for both symmetrical and antisymmetrical aperture antennas. Antennas Propag IEEE Trans 37(8):990–995
Costanzo S, Di Massa G (2002) An integrated probe for phaseless near-field measurements. Measurement 31(2):123–129
Costanzo S, Di Massa G (2004) Far-field reconstruction from phaseless near-field data on a cylindrical helix. J Electromagn Waves Appl 18(8):1057–1071
Costanzo S, Di Massa G (2007) Near-field to far-field transformation with planar spiral scanning. Prog Electromagn Res 73:49–59
Costanzo S, Di Massa G, Migliore D (2005) A novel hybrid approach for far-field characterization from near-field amplitude-only measurements on arbitrary scanning surfaces. Antennas Propag IEEE Trans 53(6):1866–1874
D'Agostino F, Ferrara F, Gennarelli C, Riccio G, Savarese C (2002) NF-FF transformation with cylindrical scanning from a minimum number of data. Microwave Opt Technol Lett 35(4):264–270
D'Agostino F, Gennarelli C, Riccio G, Savarese C (2003) Data reduction in the NF-FF transformation with bi-polar scanning. Microwave Opt Technol Lett 36(1):32–36
D'Agostino F, Gennarelli C, Riccio G, Savarese C (2006) Theoretical foundations of nearfield – far-field transformations with spiral scannings. Prog Electromagn Res 61:193–214
D'Agostino F, Ferrara F, Gennarelli C, Guerriero R, Migliozzi M (2008a) Near-field – far-field transformation technique with helicoidal scanning for elongated antennas. Prog Electromagn Res B 4:249–261
D'Agostino F, Ferrara F, Gennarelli C, Guerriero R, Migliozzi M (2008b) An effective NF-FF transformation technique with planar spiral scanning tailored for quasi-planar antennas. Antennas Propag IEEE Trans 56(9):2981–2987
D'Agostino F, Ferrara F, Gennarelli C, Guerriero R, Migliozzi M (2009a) Laboratory tests assessing the effectiveness of the NF-FF transformation with helicoidal scanning for electrically long antennas. Prog Electromagn Res 98:375–388
D'Agostino F, Ferrara F, Fordham J, Gennarelli C, Guerriero R, Migliozzi M, Riccio G, Rizzo C (2009b) An effective near-field – far-field transformation technique for elongated antennas using a fast helicoidal scan [measurements corner]. Antennas Propag Mag IEEE 51(4):134–141
D'Agostino F, Ferrara F, Gennarelli C, Guerriero R, Migliozzi M, Riccio G (2009c) A nonredundant near-field to far-field transformation with spherical spiral scanning for nonspherical antennas. Open Electr Electron Eng J 3:1–8
D'Agostino F, Ferrara F, Gennarelli C, Guerriero R, Migliozzi M, Riccio G (2009d) Near field – far-field transformation techniques with spiral scannings. CUES, Salerno
D'Agostino F, Ferrara F, Gennarelli C, Guerriero R, Migliozzi M (2009e) The unified theory of near-field-far-field transformations with spiral scannings for nonspherical antennas. Prog Electromagn Res B 14:449–477

D'Agostino F, Ferrara F, Gennarelli C, Guerriero R, Migliozzi M (2011) Effective antenna modellings for NF-FF transformations with spherical scanning using the minimum number of data. Int J Antennas Propag 2011, 936781, 11 pages

D'Agostino F, Ferrara F, Gennarelli C, Gennarelli G, Guerriero R, Migliozzi M (2012a) On the direct non-redundant near-field-to-far-field transformation in a cylindrical scanning geometry. Antennas Propag Mag IEEE 54(1):130–138

D'Agostino F, Ferrara F, Gennarelli C, Guerriero R, Migliozzi M (2012b) An innovative direct NF-FF transformation technique with helicoidal scanning. Int J Antennas Propag 2012, 912948, 9 pages

D'Agostino F, Ferrara F, Gennarelli C, Guerriero R, Migliozzi M (2012c) Far-field reconstruction from a minimum number of spherical spiral data using effective antenna modelings. Prog Electromagn Res B 37:43–58

D'Agostino F, Ferrara F, Gennarelli C, Guerriero R, Migliozzi M (2013a) Non-redundant spherical NF-FF transformations using ellipsoidal antenna modeling: experimental assessments [measurements corner]. Antennas Propag Mag IEEE 55(4):166–175

D'Agostino F, Ferrara F, Gennarelli C, Guerriero R, Migliozzi M (2013b) Far-field reconstruction from near-field data acquired via a fast spherical spiral scan: experimental evidences. Prog Electromagn Res 140:719–732

D'Agostino F, De Colibus I, Ferrara F, Gennarelli C, Guerriero R, Migliozzi M (2014a) Far-field pattern reconstruction from near-field data collected via a nonconventional plane-rectangular scanning: experimental testing. Int J Antennas Propag 2014, 763687, 9 pages

D'Agostino F, Ferrara F, Gennarelli C, Guerriero R, Migliozzi M (2014b) Efficient reconstruction of the pattern radiated by a long antenna from data acquired via a spherical-spiral-scanning near-field facility [measurements corner]. Antennas Propag Mag IEEE 56(2):146–153

Edmonds A (1974) Angular momentum in quantum mechanics. Princeton University Press, Princeton

Ferrara F, Gennarelli C, Guerriero R, Riccio G, Savarese C (2007) An efficient near-field to far-field transformation using the planar wide-mesh scanning. J Electromagn Waves Appl 21(3):341–357

Franceschetti G (1997) Electromagnetics. Plenum Press, New York

Francis M (2012) IEEE recommended practice for near-field antenna measurements. IEEE Std 17202012:1−102

Francis M, Wittmann R (2008) Near-field scanning measurements: theory and practice, chap. 19. In: Balanis C (ed) Modern antenna handbook. Wiley, Hoboken, pp 929–976

Gatti M, Rahmat-Samii Y (1988) FFT applications to plane-polar near-field antenna measurements. Antennas Propag IEEE Trans 36(6):781–791

Gennarelli C, Riccio G, Speranza V, Savarese C (1994) Fast and accurate interpolation of radiated fields over a cylinder. Prog Electromagn Res 8:349–375

Gennarelli C, Riccio G, D'Agostino F, Ferrara F (2004) Near-field – far-field transformation techniques, vol 1. CUES, Salerno

Gennarelli C, Capozzoli A, Foged L, Fordham J, van Rensburg D (2012) Recent advances in near-field to far-field transformation techniques. Int J Antennas Propag 2012:3

Gillespie E (1988) Special issue near-field scanning techniques. Antennas Propag IEEE Trans 36(6):725–901

Gregson S, McCormick J, Parini C (2007) Principles of planar near-field antenna measurements, Electromagnetics and radar series. Institution of Engineering and Technology (IET), London

Hald J, Hansen J, Jensen F, Larsen F (1988) Spherical near-field antenna measurements. IEE electromagnetic waves series, vol 26. Peter Peregrinus, London

Hansen R (1984) Measurement distance effects on low sidelobe patterns. Antennas Propag IEEE Trans 32(6):591–594

Hansen T (2011) Spherical near-field scanning with higher-order probes. Antennas Propag IEEE Trans 59(11):4049–4059

Harrington R (1961) Time-harmonic electromagnetic fields. McGraw-Hill, New York

Hollis J, Lyon T, Clayton L, Hansen C (1972) Microwave antenna measurements. Scientific, Atlanta
Isernia T, Leone G, Pierri R (1996) Radiation pattern evaluation from near-field intensities on planes. Antennas Propag IEEE Trans 44(5):701–710
James G (1980) Geometrical theory of diffraction for electromagnetic waves. Peter Peregrinus, London
Joy E, Paris D (1972) Spatial sampling and filtering in near-field measurements. Antennas Propag IEEE Trans 20(3):253–261
Joy E, Leach WM, Rodrigue G, Paris D (1978) Applications of probe-compensated nearfield measurements. Antennas Propag IEEE Trans 26(3):379–389
Kerns D (1970) Correction of near-field antenna measurements made with an arbitrary but known measuring antenna. Electron Lett 6(11):346–347
Kerns D (1981) Plane-wave scattering-matrix theory of antennas and antenna-antenna interactions, no. 162 in NBS monograph. U.S. Government Printing Office, Washington, DC
Knab J (1983) The sampling window. Inf Theory IEEE Trans 29(1):157–159
Larsen F (1980) Probe-corrected spherical near-field antenna measurements, PhD dissertation, Technical University of Denmark, Rep. LD36
Las-Heras F, Sarkar T (2002) Radial field retrieval in spherical scanning for current reconstruction and NF-FF transformation. Antennas Propag IEEE Trans 50(6):866–874
Las-Heras F, Pino M, Loredo S, Alvarez Y, Sarkar T (2006) Evaluating near-field radiation patterns of commercial antennas. Antennas Propag IEEE Trans 54(8):2198–2207
Leach WM, Paris D (1973) Probe compensated near-field measurements on a cylinder. Antennas Propag IEEE Trans 21(4):435–445
Newell A (1988) Error analysis techniques for planar near-field measurements. Antennas Propag IEEE Trans 36(6):754–768
Newell A, Crawford M (1974) Planar near-field measurements on high performance array antennas. Nat Bur Stand (US) NBSIR 74:74–380
Papoulis A (1987) Signal analysis. McGraw-Hill, New York
Paris D, Leach WM, Joy E (1978) Basic theory of probe-compensated near-field measurements. Antennas Propag IEEE Trans 26(3):373–379
Petre P, Sarkar T (1992) Planar near-field to far-field transformation using an equivalent magnetic current approach. Antennas Propag IEEE Trans 40(11):1348–1356
Pierri R, D'Elia G, Soldovieri F (1999) A two probes scanning phaseless near-field far-field transformation technique. Antennas Propag IEEE Trans 47(5):792–802
Qureshi M, Schmidt C, Eibert T (2013) Adaptive sampling in spherical and cylindrical near-field antenna measurements. Antennas Propag Mag IEEE 55(1):243–249
Rahmat-Samii Y, Galindo-Israel V, Mittra R (1980) A plane-polar approach for far-field construction from near-field measurements. Antennas Propag IEEE Trans 28(2):216–230
Sarkar T, Taaghol A (1999) Near-field to near/far-field transformation for arbitrary near-field geometry utilizing an equivalent electric current and MoM. Antennas Propag IEEE Trans 47(3):566–573
Silver S (ed) (1984) Microwave antenna theory and design, IEE electromagnetic waves. Peregrinus, London
Stratton J (1941) Electromagnetic theory. McGraw-Hill, New York
Taaghol A, Sarkar T (1996) Near-field to near/far-field transformation for arbitrary near-field geometry, utilizing an equivalent magnetic current. Electromagn Compat IEEE Trans 38 (3):536–542
Wacker P (1975) Non-planar near field measurements: spherical scanning. NBSIR 75-809, Boulder
Whittaker E (1915) On the functions which are represented by the expansions of the interpolation theory. Proc R Soc Edinb 35:181–194
Williams L, Rahmat-Samii Y, Yaccarino R (1994) The bi-polar planar near-field measurement technique, part I: implementation and measurement comparisons. Antennas Propag IEEE Trans 42(2):184–195

Yaccarino R, Rahmat-Samii Y (1999) Phaseless bi-polar planar near-field measurements and diagnostics of array antennas. Antennas Propag IEEE Trans 47(3):574–583
Yaccarino R, Rahmat-Samii Y, Williams L (1994) The bi-polar planar near-field measurement technique, part II: near-field to far-field transformation and holographic imaging methods. Antennas Propag IEEE Trans 42(2):196–204
Yaccarino R, Williams L, Rahmat-Samii Y (1996) Linear spiral sampling for the bipolar planar near-field antenna measurement technique. Antennas Propag IEEE Trans 44(7):1049–1051
Yaghjian A (1975) Upper-bound errors in far-field antenna parameters determined from planar near-field measurements. Part 1: analysis, National Bureau Standards(US), Technical Note 667, 76
Yaghjian A (1977) Near-field antenna measurements on a cylindrical surface: a source scattering matrix formulation, NBS Tech. note 696, U.S. Government Printing Office, Washington, DC
Yaghjian A (1986) An overview of near-field antenna measurements. Antennas Propag IEEE Trans 34(1):30–45
Yaghjian A, Wittmann R (1985) The receiving antenna as a linear differential operator: application to spherical near-field scanning. Antennas Propag IEEE Trans 33(11):1175–1185
Yaghjian A, Woodworth M (1996) Sampling in plane-polar coordinates. Antennas Propag IEEE Trans 44(5):696–700